Hydraulic characterization of an unsaturated vegetated soil: The role of plant roots and hydraulic hysteresis

Ana Sofia A. S. Dias, Marianna Pirone, Marco Valerio Nicotera, Gianfranco Urciuoli

Version of Record: https://www.sciencedirect.com/science/article/pii/S2352380821000034
Manuscript_074d36b2f72b89ac34e714eb37c726e3

Hydraulic characterization of an unsaturated vegetated soil: the role of plant roots and hydraulic hysteresis

Ana Sofia Dias[a,b,c], *Marianna* Pirone[a], *Marco Valerio* Nicotera[a], and *Gianfranco* Urciuoli[a]

[a]Department of Civil, Architectural and Environmental Engineering, Università di Napoli Federico II, Via Claudio 21, 80125 Naples, Italy

[b]University of Montpellier, AMAP, INRAE, IRD, CNRS, CIRAD, 34000 Montpellier, France

[c]Department of Engineering, Durham University, DH1 3LE, Durham, UK

ana.s.dias@durham.ac.uk

marianna.pirone@unina.it

nicotera@unina.it

gianurci@unina.it

Corresponding author:

Ana Sofia Dias

Department of Engineering, Durham University

Lower Mountjoy, South Road, Durham, DH1 3LE, UK

Tel: +44 077 188 716 59

ana.s.dias@durham.ac.uk

Hydraulic characterization of an unsaturated vegetated soil: the role of plant roots and hydraulic hysteresis

Abstract

Flowslides and debris flows in granular soils pose a serious threat to human life and man-made structures. Due to rainwater infiltrating into superficial unsaturated soils, rainfall is the most common triggering factor of such landslides, causing a decrease in matric suction and hence in soil shear strength. Early warning systems based on accurate analyses of groundwater response to meteorological factors are widely used to mitigate landslide risk. In such a context, the accuracy of the model adopted to calculate the groundwater field is closely related to the reliability and meaningfulness of hydraulic soil characterization. In this paper, an extensive laboratory investigation regarding the hydraulic behaviour of pyroclastic unsaturated deposits from a vegetated slope monitored on Mount Faito (Campania, Southern Italy) is presented to highlight the importance of hydraulic hysteresis and the presence of roots in shallow soils. Water retention properties and hydraulic conductivity functions were determined, focusing on a drying-wetting cycle. Tests on specimens sampled in the top ten centimetres of the soil profile were also carried out to assess the effects of plant roots on soil hydraulic properties. Inverse analyses were used to estimate the parameters of a hysteretic hydraulic model. Finally, parametric numerical analyses, carried out via a finite element code, were used to highlight the potential effects of the hydraulic characterization on the stability of sloping pyroclastic covers, including all above factors.

Keywords: unsaturated soil; hydraulic soil characterization; pyroclastic soil; hydraulic hysteresis; rooted soil

1 Introduction

Flowslides and debris flows can lead to huge human and economic losses. Rainfall is the most usual trigger of such landslides, resulting from rainwater infiltration into unsaturated subsoil that induces a decrease in matric suction and hence in soil shear strength. Flowslides and debris flows occur widely in many geological settings, such as crystalline bedrocks covered by uppermost weathered soils[1,2], eluvial and colluvial covers on clay shales[3,4] and pyroclastic soils resting on igneous, carbonate or flysch bedrock in the vicinity of volcanoes[5-17]. Several flowslides have occurred in shallow pyroclastic deposits resting on steep slopes in the areas surrounding Mount Vesuvius (Campania, Southern Italy) in the last twenty years, as the tragic events in Sarno (1998), Nocera (2005) and Ischia (2006).

Early warning systems, based on accurate analysis of the groundwater regime and its relationship with meteorological factors, are widely used as a measure for forecasting and mitigation of rapid landslide risk[18]. In this framework, physically-based models are required to correctly reproduce the hydro-mechanical behaviour of unsaturated slopes through numerical analyses. Reliable predictions of matric suction and volumetric water content in sloping subsoil can be obtained by considering the hysteretic hydraulic behaviour of the soil and the effects of vegetation on soil hydraulic properties.

Accounting for the hysteresis of the water retention curve (WRC) and the hydraulic conductivity function (HCF) produces a better estimation of the propagation of wetting fronts during heavy rainfall[19]. Recent studies[13,20] considered the hysteretic hydraulic soil response in such contexts. Comegna et al[13] investigated the influence of rainwater infiltration on hydraulic soil response and hence on slope stability conditions, stressing the potential errors in the prediction of landslide triggering when hydraulic hysteresis is neglected.

The effect of vegetation on soil hydraulic properties has been investigated only recently in the geotechnical literature. Plant roots change the soil fabric progressively, which affects soil hydraulic properties[21]. Several experimental works by Leung et al[22], Ng et al[23,24] and Ni et al[25,26] have shown that the presence of roots affects the shape of both soil WRCs and HCFs. Ng et al[24] and Ni et al[26] found that the presence of one plant species generally provides a reduction in saturated soil permeability compared to that of bare soil whereas mixed-species and/or high plant density lead to an increase in permeability. In fact, competition among individuals leads to an increase in soil macro-porosity associated with root decay and to an increase in permeability of the root-permeated soil[27,28].

Recently, Jotisankasa et al[29], have tested the effects of Vetiver grass on the WRC and HCF in two types of soils: a low plasticity silt and a clayey sand. They found that roots disturb the pore-size distribution of vegetated soil in the range of macro-pores greater than about 1.5 mm, and hence affect soil hydraulic properties mainly in the range of matric suction values lower than 1 kPa. In particular, in low plasticity silt, for root densities lower than 6.5 kg/m^3, saturated permeability values increased up to 2 to 5 times of those of bare soils, mainly due to desiccation cracks and preferential flow induced by drying and wetting cycles. On the contrary, for root densities higher than the aforementioned threshold, permeability values decreased due to the obstruction of macro-voids caused by roots.

Jotisankasa et al[29] identified four main phenomena occurring during plant growth affecting soils hydraulic conductivity: i) cycles of wetting and drying due to plant watering and evapotranspiration; ii) decay of roots that generates preferential flow paths along the impoverished roots; iii) obstruction of macro-pores by plant roots; and iv) organic carbon released by plant (the so-called root exudation). The first two phenomena provide an increase in saturated hydraulic conductivity values, the third one a decrease. Then, the fourth phenomena generate an increment of the saturated volumetric water content. The combined effects due to all these features simultaneously is hardly quantifiable over root growth and these change with the soil type, the plant species and their interaction.

Within this interpretative framework, the paper reports the results of extensive hydraulic experimentation carried out in laboratory on pyroclastic soil samples, with and without roots, collected at a test site on Mt. Faito (Campania, Southern Italy), close to an area involved in several flowslide phenomena. The experimental technique used in this research was developed for pyroclastic soil of the same regional context by Nicotera et al[30] who determined drying paths of WRCs and HCFs; however, in this case the study was extended to wetting paths too.

Each specimen was subjected to a saturated hydraulic conductivity test at constant head and to some drying-wetting cycles. Inverse analyses of measurements for each laboratory test were carried out with a finite element method code, HYDRUS-1D, in order to estimate hydraulic model parameters for main drying (MDC) and main wetting (MWC) branches of WRC and HCF. Furthermore, the model of Parker and Lenhard[31] was adopted to interpret the hydraulic hysteresis.

Lastly, some results of numerical analyses are shown to assess the effects of hydraulic hysteresis and roots presence on matric suction and water content distribution along a soil column during heavy rainfall. The response to rainfall was modelled with reference to a soil column typical of the test site at

Mt. Faito (Campania, Southern Italy), varying the initial soil condition and the duration of heavy rainfall.

2 Test site

The investigated soils belong to the pyroclastic cover of the Lattari Mountains on the Sorrento Peninsula in Campania (southern Italy). Several flowslides, debris flows and debris avalanches have occurred on the Lattari Mts. and in the surrounding areas, such as in Pagani (1972), Pozzano (1997), Nocera (2005), and more recently Vico Equense (2018)[16]. The study area is located at an altitude of about 850 m on a North-facing slope of Mt. Faito (40°40'32.29"N, 14°28'23.35"E) (Figure 1a). Mature individuals of *Castanea sativa* Mill. are cultivated in this area for fruit production. The understory is mostly composed of ferns (*Pteridium aquilinum*) and shrubs (e.g. *Rubus ulmifolius* and *Corylus avellana*). Vegetation starts to grow in mid-April, reaching its peak in July, and dries out in November. Trees become dormant during the wet season when trees shed leaves, forming a groundcover mostly consisting of dried leaves.

The stratigraphic profile observed in the field is composed of a series, 2.5 m thick, of pyroclastic soils resting on fractured limestone. These soil layers are attributable to two different explosive volcanic falls: (i) the shallower younger soil dates to the 79 AD eruption of Mt. Vesuvius; (ii) the deeper older layers are of uncertain origin, but preliminary tephro-stratigraphic data attribute them to a Phlegraean eruption occurring around 130,000 years ago[32]. From top to bottom, the stratigraphic sequence consists of the following layers (Figures 1b-e)[16]:

- layer A, the topsoil; the upper part of this layer, called A1 (0.20-0.30 m thick), is affected by biogeochemical processes due to the action of microorganisms and vegetation; the lower part, A2 (0.40-1.00m thick), is an ash consisting of pumice-rich silty sand;
- layer B, which consists of coarse ungraded white pumices (gravel particles with a diameter of 20-40 mm), in a fine sandy pyroclastic matrix; the thickness is quite variable, ranging between 0.5 and 1.2 m;
- layer C, whose upper part is attributed to an ancient Phlegraean pyroclastic fall, referred to as C1 (0.40-0.80 m thick), made of yellowish silty sands; the lower part, C2, consisting of highly weathered reddish-brown ash (silty sand), with a clayey fraction, has a very variable thickness (0.20–1.20 m), and in some areas of the test site is discontinuous.

2.1 Soil physical properties

Grain size analyses, according to the Unified Soil Classification System[33] were carried out on samples taken in all the layers of the soil cover at the test site (Figures 1f-i). The shallower soils, layers A1 and A2, were classified as silty sand with gravel and silty gravel with sand, respectively; layer B as well-graded gravel with sand; the bottom soils, C1 and C2, as sandy silts.

The values of soil physical properties determined on the undisturbed specimens used for hydraulic characterization are reported in Table 1. Only ash layers in the cover were investigated: topsoil, layers A1 and A2, and bottom soil, layers C1 and C2. In addition, some specimens were collected at the ground surface in order to better characterize the roots effect of on hydraulic properties. Hereafter this layer, whose thickness is 0.10 m, will be called A1sup. Specific gravity of soil particles (G_s) was obtained according to ASTM standard[34]; G_s values ranges from 2.52 to 2.69 along the vertical soil profile (Table 1). Fines fraction presents in soil layers A and B was not plastic. Instead fine fraction in soil C2 provided a plastic limit varying between 23% and 60 % and a plasticity index ranging between 3% and 17 %, thus, this soil is classified as medium and high compressibility silt[35].

Table 1. Soil physical properties and root information of each tested specimen: sampling depth (z), soil particle specific gravity (G_s), soil dry density not accounting for the presence of roots (γ_d), soil porosity of bare soil (n_0), root dry biomass (M_{roots}), root volume ratio (R_v), and root-permeated soil porosity (n).

Soil layer	Sample no.	z [m]	G_s [-]	γ_d [g cm^{-3}]	n_0 [-]	M_{roots} [g]	R_v [-]	n [-]
A1sup	N1	0.05	2.580	0.8935	0.654	0.484	0.00503	0.649
A1sup	N2	0.05	2.580	0.8020	0.689	0.340	0.00352	0.686
A1sup	R1	0.05	2.515	0.7393	0.713	2.471	0.02521	0.688
A1sup	R2	0.05	2.580	0.7760	0.699	1.176	0.01206	0.687
A1sup	R3	0.20	2.580	0.8193	0.682	0.962	0.00988	0.673
A1sup	R4	0.00	2.580	0.7469	0.711	1.840	0.01869	0.692
A1sup	R5	0.00	2.580	0.6556	0.746	4.630	0.04617	0.700
	mean	**0.06**	**2.570**	**0.7761**	**0.699**	**1.700**	**0.01722**	**0.682**
	std. dev.	**0.07**	**0.025**	**0.0742**	**0.029**	**1.491**	**0.01484**	**0.017**
A1	1.11.1	0.50	2.603	0.9265	0.644	0.274	0.00286	0.641
A1	1.11.2	0.50	2.603	1.0017	0.615	0.056	0.00059	0.615
A1	1.6.2	0.80	2.688	0.8690	0.677	0.098	0.00102	0.676
A1	1.7.2	0.80	2.580	0.9950	0.614	0.133	0.00138	0.613
A1	1.9.1	0.50	2.580	0.8217	0.681	1.337	0.01371	0.668
A1	1.9.2	0.50	2.580	0.8937	0.654	0.627	0.00648	0.647
	mean	**0.60**	**2.606**	**0.9179**	**0.648**	**0.421**	**0.00434**	**0.643**
	std. dev.	**0.15**	**0.042**	**0.0711**	**0.029**	**0.495**	**0.00507**	**0.026**
A2	1.1.1	1.65	2.688	0.8053	0.700	0.072	0.00074	0.700
A2	1.2.1	1.65	2.688	0.7379	0.725	0.128	0.00132	0.724
A2	1.4.1	1.65	2.688	0.9838	0.634	0.052	0.00054	0.633
A2	1.5.1	0.95	2.688	0.7731	0.712	0.071	0.00073	0.712
A2	1.5.2	0.95	2.688	0.8630	0.679	0.049	0.00051	0.678

A2	1.6.1	0.80	2.688	0.8075	0.700	0.098	0.00102	0.699
A2	1.7.1	0.80	2.688	0.7650	0.715	0.086	0.00089	0.714
	mean	**1.21**	**2.688**	**0.8194**	**0.695**	**0.079**	**0.00082**	**0.694**
	std. dev.	**0.42**	**0.000**	**0.0827**	**0.031**	**0.028**	**0.00028**	**0.031**
C1	2.12.1	1.45	2.666	0.6654	0.750	-	-	0.750
C1	2.12.2	1.45	2.666	0.7143	0.732	0.360	0.00371	0.728
C1	2.13.1	1.30	2.646	0.6413	0.758	0.077	0.00080	0.757
C1	2.15.1	1.30	2.666	0.6701	0.749	0.098	0.00102	0.748
C1	3.16.1	1.10	2.624	0.9840	0.625	-	-	0.625
	mean	**1.32**	**2.656**	**0.7350**	**0.723**	**0.178**	**0.00184**	**0.722**
	std. dev.	**0.14**	**0.019**	**0.1417**	**0.055**	**0.158**	**0.00162**	**0.055**
C2	1.1	1.80	2.528	0.8064	0.681	0.064	0.00066	0.680
C2	1.2	1.80	2.455	0.9036	0.643	0.951	0.00984	0.633
C2	1.3	0.80	2.528	0.7831	0.690	0.386	0.00399	0.686
	mean	**1.47**	**2.500**	**0.8310**	**0.671**	**0.467**	**0.00483**	**0.666**
	std. dev.	**0.58**	**0.042**	**0.0639**	**0.025**	**0.449**	**0.00465**	**0.029**

The investigated deposits presented high porosities (n_0), ranging from 0.61 to 0.76 (Table 1). Additionally, the specimens were extremely permeated by roots; the roots present in the samples were dead and unable to affect the soil matric suction through transpiration. Hence, the model of Ng et al[24] was adopted to better estimate soil porosity as the solid phases in the samples was composed by soil particles and roots characterized by two different densities. Hence the root-permeated soil porosity n was estimated as:

$$n = n_0 - R_v \quad (1)$$

where n_0 is the porosity of bare soil, and R_v is the root volume ratio (Table 1). The root volume ratio (R_v) is defined as the ratio between the volume occupied by roots in a root-permeated soil specimen and the total volume of the specimens itself. In this case, R_v was estimated for each cylindrical soil sample (diameter = 71.5 mm; height = 60 mm; volume = 240.90 cm^3) recovered in situ. First of all, the dry biomass in each soil sample (M_{roots}) was determined by collecting individually the roots after oven-drying the rooted samples at 105 °C for 24 h and measuring their weight in a precision scale with an accuracy of 0.001 g. Then, the volume occupied by roots was calculated as the ratio between M_{roots} and the specific gravity of roots.

The specific gravity of the roots of *C. sativa* was first determined[35]: analyses of the digital images of roots were carried out with the software WinRHIZO (Regent Instruments, Inc) to estimate their volume. The specific gravity of root wood depends on root moisture content[36]. In the present study, matric suction varied between 0 and 100 kPa, in this range wood moisture content would be equal to about 23 % and root volume changes are not expected, according to Simpson and Ten

Wolde[36].Therefore, the root specific gravity is fairly constant in the matric suction range experienced by soil samples and it resulted equal to 0.399.

Soil porosity value estimated according to equation 1 is about 2.5% lower than that estimated by neglecting the pore volume occupied by roots in the surficial layer A1sup. The difference between the two porosity values is lower in the remaining soil layers.

3 Methods

3.1 Experimental procedure

The experimental procedure consisted of a sequence of laboratory tests to collect data about: a) saturated hydraulic conductivity; b) development over time of soil response during evaporation and imbibition processes, at both (b1) low to medium matric suction values (i.e. from 0 to 80 kPa, largely bounding the expected AEV of tested soils,), and (b2) high matric suction values (i.e. corresponding to water content values close to the residual one, with matric suction values from 800 kPa up to 1.0 MPa). Data indicated in point b) were obtained using two different laboratory devices: a ku-pf MP10 apparatus for low to medium matric suction values (b1) and a pressure plate for high matric suction values (b2). The results of both drying and wetting tests carried out in the b-range were used to calibrate a K-P-S (hydraulic conductivity – pore pressure – saturation) hysteretic model.

Each soil specimen was trimmed from an undisturbed and unsaturated soil core directly into a cylindrical stainless-steel sleeve (whose diameter and length were respectively 71.5 mm and 60.0 mm) and weighed to record its initial state (i.e., water content and porosity). The device used to perform permeability tests (phase a) was equipped with: (i) pressure probes, to measure pore water pressure at the bottom and top of the specimen, (ii) two water reservoirs with pressure regulators, and (iii) two burettes to control the water volume flowing through the specimen. Distilled water was flushed upwards through the specimen by applying 10 kPa and 5 kPa in the lower and upper reservoir, respectively. Volumes of water flowing into and out of the soil specimen were monitored over time. At the steady state, when inflow and outflow rates became equal, full saturation of the specimen was supposed to be attained. At least four flushing cycles were repeated per test. The permeability of the soil specimen inferred from data collected during the steady phase of the test was considered a good estimate of the saturated permeability.

At the end of the permeability test, the specimens still contained in the steel sleeve were moved for the b1 phase to a ku-pf MP10 apparatus (Umwelt-Geräte-Technik GmbH, Figure 2), consisting of a star-

184 shaped sampler changer which managed up to ten stainless steel specimen rings, in order to monitor
185 matric suction and water content during evaporation and imbibition cycles.
186 A plastic paraffin film (parafilm M) was fixed at the bottom of the sample to prevent water evaporation
187 and drainage. The matric suction in each specimen was measured at two points (15 mm and 45 mm
188 below the top of the sample) by means of two mini-tensiometers, with a full-scale of 80 kPa and a
189 measurement resolution of 0.01 kPa. The mini-tensiometers were preliminarily saturated and calibrated
190 following standard procedures and then carefully installed in prearranged holes in order to ensure good
191 contact between the porous tip and the soil specimen. Each pair of tensiometers was connected to a
192 conditioning unit arranged upon each sample holder. The star-shaped changer periodically placed each
193 sample holder upon a precision balance (resolution of 0.01 g) and variations in total soil water storage
194 were determined from weight measurements. Matric suction and weight measurements were recorded
195 every 10 minutes throughout the entire test, i.e. wetting and drying phases. For more details about the
196 ku-pf apparatus readers can refer to Nicotera et al[30].
197 The saturated soil specimens contained in the rings were sealed also at the top end and were placed on
198 the specimen holders waiting for the hydrostatic condition to be reached. Hydraulic equilibrium was
199 checked via tensiometer readings, assuming that the equalization process was complete when the
200 difference between the top and bottom tensiometer measurements decreased to 0.3 kPa (i.e.,
201 corresponding to the hydrostatic matric suction profile).
202 The evaporation phase was initiated by removing the sealing cap and cling film from the top of the
203 sample: this way, water started to evaporate from the top surface of the sample. When the main drying
204 branch of the WRC had to be determined, drying process was stopped before tensiometers cavitation
205 (i.e. when matric suction readings reached the range between 70 kPa and 80 kPa) by covering the
206 sample with clinging film and a metallic cap. If the scanning paths were detected, the drying process
207 was stopped at reversal points corresponding to matric suction varying between 20 kPa and 50 kPa.
208 Subsequently, the soil sample was subjected to a series of wetting steps: distilled water was repeatedly
209 manually poured onto the top surface of the sample and infiltrated into the specimen, redistributing in
210 the soil. Different masses of water were used in each step: a larger mass of 5 g was added when the
211 matric suction values measured in the sample exceeded 15 kPa; a mass of 3 g of water was added,
212 instead, if the matric suction values were lower than 15 kPa. It was thus possible to obtain more refined
213 water retention data around the air-entry value (AEV) of the WRC, which ranged approximately from

6 kPa up to 12 kPa[30]. During each step of wetting, the soil sample top surface was covered with a clinging film and a cap to prevent evaporation as much as possible. Each new wetting step started after the attainment of hydrostatic condition in the sample and lasted at least two hours. In this regard, it is useful to highlight that two hours was the minimum necessary time to reach the equilibrium in a wetting step. Indeed, the equilibrium was reached quickly when the sample was close to saturation because the hydraulic conductivity was high and a quick movement of water inside the sample occurred. Furthermore, the height of samples was small (60 mm) and small quantities of water were added in the low suction range (3g). However, the hydrostatic conditions can take as much as three days to be reached when suction is high.

In the range of residual saturation, there is a significant change in the gradient of the WRC: large increases in matric suction produce small decreases in water content[37]. Investigation of the water retention properties in this region requires measurement of matric suctions significantly higher than 80 kPa and hence well above the full-scale value of the ku-pf mini-tensiometers. A pressure plate apparatus was used to determine water contents along the main drying branch in the range of residual saturation by applying matric suction values of 600 kPa or 850 kPa through the axis translation technique (b2 phase). In the present work, only one point of the WRC per tested specimen was determined by means of the pressure plate in accordance with the procedure suggested by Nicotera et al[30]. The samples were removed from the baskets of the ku-pf apparatus after the end of the last drying phase. The bottom surface of the samples was placed on the porous stone of the pressure plate assuring good contact. The weight of the samples was recoded using a balance. The experimental procedure was concluded by oven-drying the sample to determine water content, porosity and root dry biomass.

The procedure discussed in this study does not involve measurements of soil volume variation. However, the volume changes due to water content variations in pyroclastic soils of this region, at least for the surficial layers (A), are expected to be non-significant according to previous experimental work on pyroclastic soils of the same region[38,39].

3.2 Evaluation of the parameters of the hydraulic hysteretic model

The hysteretic model adopted herein was proposed by Lenhard et al[40] and is implemented in HYDRUS-1D software[41]. The relationship between the volumetric water content (θ) and the matric suction (s) is described by the classical van Genuchten[42] equation. However, two different sets of

values of the fitting parameters are required to describe WRC along main-drying and main-wetting represented by Equation 2 and 3, respectively:

$$\theta(s) = \theta_r + (\theta_s^d - \theta_r)/\left\{[1 + (\alpha^d s)^{n_v}]^{1-1/n_v}\right\} \quad (2)$$

$$\theta(s) = \theta_r + (\theta_s^w - \theta_r)/\left\{[1 + (\alpha^w s)^{n_v}]^{1-1/n_v}\right\} \quad (3)$$

where the superscripts *d* and *w* refer to the main drying and main wetting curves, respectively; θ_r is the residual volumetric water content; α and n_v are fitting parameter of the van Genuchten equation; θ_s represents the volumetric water content at saturation.

In this study the WRC and HCF have been assumed unimodal for each layer. However, in the last findings of Jotisankasa et al[29] on the effects of Vetiver grass on the hydraulic behaviour of clayey sand, the HCF shows a bi-modal trend probably due to the plant variation.

The differences between the two curves are related to the maximum value θ_s of the volumetric water content and to the matric suction scaling parameter (α). Two different values for both parameters are considered for drying and wetting, respectively θ_s^d and $\theta_s^w$and α^d and α^w. The fitting parameter n_v and the residual water content (θ_r) are the same for both branches.

The scanning paths are scaled from the main branches following the method presented by Parker and Lenhard[31], characterized by a closed hysteretic loop. In particular, drying scanning curves are scaled from the main drying curve, and wetting scanning curves from the main wetting curve. The scaling procedure is well documented in Rianna et al[20] and Vogel et al[43]. Compared to other models based on a scaling procedure, this model allows prevention of the artificial pumping error, that is, the non-closure of the scanning loops in simulated cyclic paths, which is considered to be an aberration rather than a soil property. This is avoided by collecting in the model all the reversal points experienced by the soil. Preserving the "memory" of the various wetting–drying cycles to which the sample has been subjected allows paths to draw closed scanning loops.

The HCF is modelled in HYDRUS-1D according to Vogel et al[43]. It is described by Equation 4, where K is the soil hydraulic conductivity, l and m are fitting parameters, in which $m = 1 - 1/n_v$, S is the effective degree of saturation (Equation 5), and K_{sat} is the saturated hydraulic conductivity[42,44].

$$K(S) = K_{sat} S^l \left[1 - \left(1 - S^{1/m}\right)^m\right]^2 \quad (4)$$

$$S = (\theta - \theta_r)/(\theta_s - \theta_r) \quad (5)$$

The model parameters were estimated via inverse analysis of the experimental measurements. According to Nicotera et al[30], application of the inverse method consists of a numerical analysis

simulating a lab test, and determination of the values of the model parameters for which differences between observed and simulated flow variables are minimized; the estimated values of the parameters are those that optimize the model response[45]. This procedure was carried out in this research through the software HYDRUS-1D in which an objective function was minimized by using the Levenberg-Marquardt non-linear method[46].

The fitting of the hysteretic model was subdivided into two subsequent phases: the first consisted of fitting the parameter vector associated to the main drying branch ($\theta_s^d, \theta_r, \alpha^d, n_v, l$); the second phase was devoted to estimating the remaining parameters associated to the main wetting branch (θ_s^w, α^w).

The fitting of the main drying curve followed the procedure defined by Nicotera et al[30]. In particular, the data sets in the objective function were composed by: (i) the matric suction values measured by the two mini-tensiometers during the evaporation process; (ii) a data pair (s, θ) obtained from the final readings in the pressure plate; and (iii) a data pair (s, θ) corresponding to AEV. AEV was identified as the point of maximum curvature on the WRC curve preliminarily obtained by coupling the arithmetic mean of the two measurements of matric suction to the average water content of the whole soil sample. Initial guesses of the parameters were determined by fitting the experimental points by the van Genuchten equation using the Solver function of Excel in order to minimize the coefficient of determination. In the inverse analyses, the parameters θ_s^d and θ_r were allowed to vary between 0 and 1, the parameters α^d and n were allowed to vary between 0 and 10 (kPa^{-1} in the case of α^d), and the parameter l was allowed to vary between -10 and 10, as suggested by Nicotera et al[30].

Regarding the wetting branch, the data set in the objective function was composed of the matric suction values measured by the two tensiometers over one drying-wetting cycle, as suggested in Dias[35]. The initial guess for α^w and θ_s^w were set equal respectively to $2\alpha^d$ and to the average water content of the soil sample at the end of the wetting process as inferred from the weight of the sample itself. The optimal values of θ_s^w and α^w were searched in the range from 0 to θ_s^d and from 0 to 100 kPa^{-1}, respectively.

3.2.1 Water capacity

Once the fitting parameters had been determined, water capacity associated to the main loop was determined. Water capacity (C), or water storage modulus, is the derivative of the WRC (Equations 2

and 3), resulting in the following general equation[47] valid for both drying and wetting branches according to the values assumed for parameters θ_s and α:

$$C = d\theta/ds = \alpha(\theta_s - \theta_r)(n_v - 1)|\alpha \cdot s|^{n_v-1}(1 + |\alpha \cdot s|^{n_v})^{1/n_v-2} \quad (6)$$

Water capacity regulates the propagation velocity of the wetting front in the subsoil: the higher the water capacity, the slower is the wetting front movement. Indeed, Freeze[48] observed experimentally that, in sands, keeping the saturated permeability constant, higher water capacity results in less water flowing towards deep soils because a large amount of water needs to satisfy the storage demand by the soil.

4 Results

4.1 Saturated hydraulic conductivity

Saturated hydraulic conductivity, measured in the laboratory according to the previous procedure, varies by slightly above one order of magnitude along the vertical profile, ranging from $1.69 \times 10^{-7} ms^{-1}$ to $8.09 \times 10^{-6} ms^{-1}$ (Table 2). These values compare well with those measured on pyroclastic soils sampled at other test sites in Campania[30,49]. It is worth noting that permeability values determined at the end of the saturation phase reported in Table 2 should be considered only a lower limit for saturated permeability (K_s) because the full saturation of specimens was not always attained.

Table 2. Values of Mualem–van Genuchten model parameters derived via inverse analysis of the first drying phase.

soil	sample	z (m)	$K_{sat}^d (m\ s^{-1})$	θ_r	θ_s^d	α^d (kPa^{-1})	n_v	l	AEV (kPa)	R^2
A1 sup	R1	0.05	8.09E-06	0.160	0.677	0.1680	1.580	1.795600	2.5964	0.983
	R2	0.05	3.70E-06	0.139	0.635	0.1401	1.490	1.639600	3.0935	0.998
	R3	0.05	6.21E-06	0.117	0.625	0.1647	1.525	0.719800	2.5932	0.999
	N1	0.05	4.35E-07	0.120	0.610	0.0750	1.546	0.677320	5.7970	1.000
	N2	0.20	4.35E-07	0.132	0.588	0.1045	1.551	0.000103	4.1623	1.000
	mean	0.00	**2.04E-06**	**0.134**	**0.627**	**0.1304**	**1.538**	**0.966485**	**3.648**	
	std dev	0.00	**-**	**0.017**	**0.033**	**0.0401**	**0.033**	**0.744795**	**1.3609**	
A1	1.6.2	0.06	(4.35E-07)	0.143	0.569	0.1068	1.725	0.000001	4.1733	1.000
	1.7.2	0.07	2.93E-07	0.051	0.569	0.0533	1.515	2.398400	8.1397	0.999
	1.9.1	0.50	9.02E-07	0.161	0.644	0.1109	1.772	0.038050	4.0539	0.999
	1.9.2	0.50	6.02E-07	0.089	0.606	0.0874	1.424	1.451900	4.9648	0.997
	1.11.2	0.80	(4.35E-07)	0.105	0.521	0.0883	1.492	1.197200	4.9086	0.998
	mean	0.80	**4.96E-07**	**0.110**	**0.582**	**0.0893**	**1.586**	**1.017110**	**5.2480**	

	std dev	0.50	**-**	**0.044**	**0.046**	**0.0228**	**0.153**	**1.015198**	**1.6686**	
A2	1.1.1	0.50	(1.43E-06)	0.080	0.597	0.1315	1.510	-0.466950	3.2983	1.000
	1.2.1	0.60	(1.43E-06)	0.104	0.580	0.1192	1.585	0.217510	3.6614	0.999
	1.4.1	0.15	1.43E-06	0.120	0.453	0.0604	1.768	0.933960	7.4378	0.998
	1.5.1	1.65	5.94E-06	0.082	0.549	0.0940	1.571	3.114900	4.6360	0.999
	1.6.1	1.65	(6.75E-07)	0.098	0.554	0.1784	1.531	0.290140	2.4342	1.000
	1.7.1	1.65	1.43E-06	0.115	0.594	0.1241	1.546	3.873900	3.5034	1.000
	mean	0.95	**1.60E-06**	**0.100**	**0.554**	**0.1179**	**1.585**	**1.327243**	**4.3346**	
	std dev	0.95	**-**	**0.016**	**0.054**	**0.0394**	**0.094**	**1.752830**	**1.9023**	
C1	2.12.2	0.80	2.06E-06	0.261	0.660	0.0889	1.726	0.000108	5.0088	0.999
	2.13.1	0.80	4.88E-06	0.249	0.690	0.1141	1.778	0.006155	3.9448	0.999
	2.15.1	1.21	(6.62E-07)	0.262	0.700	0.1057	1.838	0.578340	4.3088	0.999
	mean	0.42	**1.88E-06**	**0.257**	**0.683**	**0.1029**	**1.781**	**0.194868**	**3.8999**	
	std dev	1.45	**-**	**0.007**	**0.021**	**0.0128**	**0.056**	**0.332111**	**1.1809**	
C2	1.1	1.45	5.24E-07	0.230	0.643	0.0445	1.572	0.000344	9.5787	0.997
	1.2	1.30	4.96E-07	0.103	0.630	0.0111	1.486	7.634200	39.0419	0.999
	1.3	1.30	1.69E-07	0.225	0.654	0.0242	1.667	-1.511200	18.2387	0.999
	mean	1.30	**3.53E-07**	**0.189**	**0.651**	**0.0268**	**1.581**	**0.589181**	**14.3880**	
	std dev	1.10	**-**	**0.067**	**0.007**	**0.0166**	**0.081**	**2.448492**	**15.2495**	

The negative logarithm of saturated permeability (which expresses its order of magnitude), root dry biomass, mass fraction of silt, and soil porosity of each lithotype are shown in Figures 3a-d. In Figure 3 (box and whiskers plot), each box contains the second and third quartile of the represented properties; the median value is represented by the horizontal line, the average value is indicated by an "x", and the minimum and maximum values excluding outliers are indicated by whiskers. The soil characterized by the highest mean value of permeability is A1sup, the least pervious is C2 (Table 2, Figure 3a). The saturated permeability of A1sup soil is on average one order of magnitude higher than that of A1 soil, although they have the same grain size distribution. In addition, A1sup layer presents both higher dry root biomass and higher porosity than A1 (Figure 3b). A2 layer is more permeable on average than A1, it contains a larger quantity of pumices (Figures 1f-g) but contains less dry biomass than soil A1 (Figure 3b). Therefore, the differences in terms of saturated hydraulic conductivity could be due to a combination of particle size distribution and root biomass effects. C2 layer is the least permeable on average among all the tested soil layers because of a high silt fraction and low porosity (Figures 3a-d).

4.2 Water retention curve and hydraulic conductivity function

Data collected during a test in the ku-pf apparatus on A2 soil (sample 1.4.1) are shown in Figure 4a as an example of laboratory results. In this test the soil sample was subjected to an evaporation process followed by two wetting-drying cycles. Matric suction increased during the drying phases as the water content decreased. The wetting phases consisted of a sequence of steps initiated by an abrupt increase in water content, inducing a sudden drop in matric suction measured by the top tensiometer. The pressure distribution within the soil then tended to hydrostatic condition (Figure 4b), in which the matric suction value measured by the top tensiometer (s top) was approximately 0.3 kPa higher than that measured by the bottom tensiometer (s bot). However, the volumetric water content of the sample during each wetting step remained constant but the water content distribution was not uniform within the sample. A first estimate of the WRC curve preliminarily obtained by coupling the arithmetic mean of the two measurements of matric suction to the average water content of the whole soil sample is reported in Figures 5a,c. This representation of the experimental data is based on a rather crude interpretation of data in which the laboratory specimen is assimilated to a *macroscopic volume element* and spatial variations in water content and matric suction inside it are not taken into account. However, experimental data represented in this way can be used to verify the accuracy of the inversion process. Therefore, retention curves obtained by the numerical model associating the average value of the matric suction to the average water content of the whole sample (by integrating on its whole volume water contents simulated by the model itself) are reported in Figure 5. The drying-wetting cycles measured are compared to the back-analyzed main drying and wetting branches of the WRC (Figure 5a); clearly the main loop envelops the experimental measurements. The main drying curve predicted by the model also intercepts the AEV and the data points obtained from the pressure plate (PP) (triangle and circle symbols in Figure 5a). Fitted main drying and main wetting of HCFs are reported in Figure 5b with the value of saturated hydraulic conductivity measured in the laboratory. The model satisfactorily reproduced the cycles determined experimentally: the scanning curves of the model were in good agreement with the experimental data, this also emerges from the comparison between the matric suction measurements and the values predicted over time (Figure 5c, d).

The Mualem–van Genuchten model parameters, as derived from the results of the optimization process of the first evaporation phase, are reported in Table 2. The coefficient of determination (R^2) ranges between 0.98 and 1.00. All the investigated soils behave like coarse-grained materials apart from C2

soil, AEV ranges from 2 kPa to 8 kPa (α^d varies between 0.075 and 0.17 kPa^{-1} except for soil C2; Figure 6c)[50]. The AEV is higher than 20 kPa only for C2 layer due to its fine texture (α^d varies between 0.01 and 0.04 kPa^{-1}; Figure 6c). The residual volumetric water content (θ_r) ranges approximately between 0.07 and 0.16 in soil A and between 0.10 and 0.27 in C (Figure 6a). The volumetric water content at saturation (θ_s^d) is lower in soil A than in soil C (Figure 6b) mainly due to the higher porosity. The value of parameter n_v, which affects the slope of the WRC, varies from 1.45 to 1.75 for all the soils except for C1, for which it is larger (Figure 6d). Parameter l ranges from 0.20 up to 3.00 in soils A and C1, while ranging from -1.5 to 7.00 in C2, presenting very high variability (Figure 6e).

The Mualem–van Genuchten model parameters of the MWC, as derived from the results of the optimization process, are reported in Table 3. The value of the coefficient of determination ranges from 0.85 to 0.99. Parameter θ_s^w is lower on average in soil A than in soil C (Figure 6f). The θ_s^w/θ_s^d ratio, which is an indicator of the fraction of entrapped air in the subsoil, varied from 0.84 to 1.00. The range of this ratio agrees with those reported in the literature for pyroclastic layers in other geological contexts in Campania[51,52]: 0.78-0.95. However, the air volume that remains entrapped in the voids during the wetting process depends on a multiplicity of factors such as pore-size distribution, history of drying and wetting cycles, and water supply rate[52]. In addition, it is worth pointing out that although the wetting processes in the laboratory and in situ are both directed downwards, a higher fraction of air could remain entrapped in the voids in situ, not being able to escape through the soil surface due to the higher velocity of the water infiltrating from the ground surface[53]. Among all the layers, soil A presents a higher mean value of α^w with respect to soil C (Figure 6g). The α^w/α^d ratio varied from 1.01 to 3.97 (Table 3), which is a wider range than that reported by Kool and Parker[47], which is 2.08±0.46 on average, 1.88±0.40 for undisturbed soil and 2.29±0.47 for compacted samples.

Table 3. Values of Mualem–van Genuchten model parameters of the main wetting curve derived via inverse analysis.

soil	sample	z (m)	θ_s^w	θ_s^w/θ_s^d	α^w (kPa^{-1})	α^w/α^d	R^2	K_{sat}^w (m s^{-1})
A1 sup	R1	0.05	0.565	0.84	0.1700	1.01	0.953	2.85E-07
	R2	0.05	0.598	0.94	0.2956	2.11	0.987	5.28E-07
	R3	0.05	0.607	0.97	0.2822	1.71	0.994	1.79E-06
	N1	0.05	0.610	1.00	0.2218	2.96	0.991	4.35E-07
	N2	0.20	0.587	1.00	0.2587	2.48	0.990	3.24E-07
	mean	0.00	**0.593**	**0.95**	**0.2456**	**2.05**		**5.20E-07**

	std dev	0.00	**0.018**	**0.07**	**0.0507**	**0.74**		
A1	1.6.2	0.06						
	1.7.2	0.07	0.569	1.00	0.2114	3.97	0.988	2.93E-07
	1.9.1	0.50	0.619	0.96	0.2926	2.64	0.996	3.37E-07
	1.9.2	0.50	0.520	0.86	0.2011	2.30	0.851	2.02E-08
	1.11.2	0.80						
	mean	0.80	**0.569**	**0.94**	**0.2350**	**2.97**		**2.17E-07**
	std dev	0.50	**0.049**	**0.07**	**0.0501**	**0.88**		
A2	1.1.1	0.50						
	1.2.1	0.60	0.580	1.00	0.2706	2.27	0.986	1.43E-06
	1.4.1	0.15	0.440	0.97	0.1443	2.39	0.986	5.84E-07
	1.5.1	1.65	0.549	1.00	0.2195	2.34	0.964	5.94E-06
	1.6.1	1.65						
	1.7.1	1.65	0.548	0.92	0.2146	1.73	0.991	7.10E-07
	mean	0.95	**0.529**	**0.97**	**0.2122**	**2.18**		**2.17E-06**
	std dev	0.95	**0.061**	**0.04**	**0.0519**	**0.31**		
C1	2.12.2	0.80	0.620	0.94	0.1500	1.69	0.991	4.56E-07
	2.13.1	0.80	0.675	0.98	0.2000	1.75	0.982	2.21E-06
	2.15.1	1.21						
	mean	0.42	**0.647**	**0.96**	**0.1750**	**1.72**		**1.33E-06**
	std dev	1.45	**0.039**	**0.03**	**0.0354**	**0.05**		
C2	1.1	1.45	0.618	0.96	0.0800	1.80	0.985	1.28E-07
	1.2	1.30						
	1.3	1.30						
	mean	1.30	**0.618**	**0.96**	**0.0800**	**1.80**		**1.28E-07**
	std dev	1.10						

The main loops (MDC and MWC) of each specimen, derived from the results of inverse analyses, are represented in Figures 7a-j. These detect the size of the hysteretic domain, where the paths of matric suction and water content measured in situ are usually observed[10]. Some variability is also observed among samples of the same soil.

However, during the first evaporation phase after the permeability test the state of the soil does not always follow the primary drying retention curve (corresponding to a drying process starting from perfectly saturated conditions). Hence the obtained hydraulic parameters could refer to a secondary or intermediate drying curve. In fact, fully saturation of soil specimens in the permeameter was very difficult; even after several flushing cycles, isolated air bubbles could be entrapped in the soil sample before the evaporation starts in the ku-pf apparatus. Therefore, the value of θ_s^d of the main drying curve (starting point) often was lower than the soil porosity determined on the same soil specimen, thus, the first drying did not correspond to the main drying curve. This observation is in agreement

with findings of Nicotera et al.[30] that tested the pyroclastic soils sampled from a test site in Campania Region with similar geological and geotechnical features to the test site studied here. The air entrapment preventing the fully saturation of the soil samples was observed also by Hillel[51], Lu et al.[54] and Jotisankasa and Sirirattanachat[29].

4.2.1 Discussion of the experimental results

The experimentation carried out was much more demanding than usual: the testing time required to obtain a scanning wetting curve was four times longer than the time necessary for the main drying curve.

The soil tested presented marked hydraulic hysteresis. The main wetting curve modelled by the van Genuchten model can be derived from the main drying curve by modifying only two parameters: α^w and θ_s^w. In particular, the value of α^w ranges between 1.01 and 3.97 α^d (see Kool and Parker[47]), while the value of θ_s^w ranges between 0.84 and 1.00 θ_s^d in accordance with those found elsewhere for such soils (Figure 6). Each parameter values are plotted as function of each other in the diagrams of Figure 8 in order to identify possible interplay between them. Figures 8p, r, l seem to indicate that a correlation exists between θ_r, θ_s^d and n_v in agreement with Nicotera et al.[30]; Figures 8n, j confirm the existence of a correlation between θ_s^d and θ_s^w and between α^d and α^w. Similarly, some insight of the interplay between roots amount and physical and hydraulic soil properties can be inferred from Figure 9, where n, K_{sat}^d, M_{root}, θ_s^d, and AEV are plotted each against each other. The clear dependence of the saturated hydraulic conductivity on soil porosity, as expected, emerges in Figure 9g. Indeed, θ_s^d trivially increases with soil porosity but it almost always results lower due to air entrapment (Figure 9i); the AEV increases with decreases of porosity (Figure 9j) in agreement with the results reported in literature[55,56].

In Fig. 9h porosity seems substantially independent of the M_{root} value, however the experimental data seem to be insufficiently evenly distributed along the M_{root} axis in order to reach a definitive conclusion. It is interesting to note the increase of saturated conductivity in top layer (A1 sup and A1) with dry biomass, M_{root}..This could be due to preferential flow induced by drying and wetting cycles as experienced during plant growth[29,57,58].

Again, M_{roots} is correlated to θ_s^d, at least in the top layers (Figure 9b); θ_s^d tends to increase with the amount of dry biomass, this result is in agreement with previous findings[29,59]. The θ_s^d increase with

root biomass may be attributed to the root exudation: the compound exuded around the roots tends to increase the volumetric water content near saturation. Lastly, the M_{roots} affects the AEV: in top layer, the AEV decreases (from 8 kPa to 2 kPa) with the root biomass increase (from 0.056 g up to 4.630 g). The AEV decrease in rooted soil can be a consequence of some changes in soil structure caused by roots and microbial activity in the rhizosphere because these are responsible for the formation of soil lumps (commonly referred as aggregates in ecology studies) and preferential flow channels (continuous macro-pores), so the coarse characteristics of the soil results to be amplified. An opposite trend appears for soil layer C2 but this difference is a consequence of the fact that C2 is a silty sand with a clayey fraction (more fine particles than the other soils), in addition C2 results to be the only layer for which soil porosity shows a decrease with M_{root}. Therefore, AEV decreases with root biomass because more pores are occupied by roots. Nevertheless, only three data points are available in layer C2 and hence conclusions cannot be drawn in this case.

These features highlight that the plants change the soil hydraulic properties of the soil for their benefit. The water storage capacity varies with matric suction, defining a curve decreasing towards the lower matric suctions, whose maximum occurs at a matric suction between 1 kPa and 15 kPa. For values estimated from the main drying branch, soils with lower AEV present higher water storage capacities (Figure 10a). Along the main wetting branch, the water storage capacity curves present a higher maximum (Figure 10b) with respect to the drying curves (Figure 10a). This is a consequence of the decrease in AEV from main drying to main wetting curves, while the value of parameter n_v remains constant[60].

The maximum values of water capacity estimated along both main drying and wetting branches for A1sup and A1 soils are very similar. Therefore, the rate of wetting front movement is mainly controlled by the saturated hydraulic conductivity, which is significantly different between these soils. The wetting front is expected to move faster in soil A1sup because this presents a saturated hydraulic conductivity one order of magnitude higher than A1.

5 Potential effects of hydraulic soil behaviour on soil response to rainfall

5.1 Conditions of analysis

A soil column with the hydraulic properties of the pyroclastic soil tested in this paper was modelled by using the finite element code HYDRUS-1D[43]. A series of simulations were performed to: (i) analyse

467 the effects of the presence of root-permeated soil on the propagation of the wetting front; and (ii)
468 investigate the effects of hydraulic hysteresis considering scanning paths on the response of the soil
469 column to heavy rainfall. The total length of the soil column was 0.90 m and the stratigraphy consisted
470 of A1sup layer (0.10 m thick), A1 layer (0.20 m thick) and A2 layer (0.60 m thick) (Figure 11a).
471 Four analyses, namely X1, X2, X3, and X4, were carried out by changing the hydraulic model
472 (hysteretic and non-hysteretic) and the hydraulic properties (i.e. corresponding to rooted and non-
473 rooted soil) of the most superficial layer of the soil column for a thickness of 0.10 m (Table 4). In the
474 X1 analysis, the main drying curve (MDC) was considered operative for each layer and the hydraulic
475 properties determined for A1 soil were also attributed to the upper 0.10 m of the soil column. In X2,
476 MDC determined for the A1sup layer was assigned to the first 0.10 m to take into account the root
477 presence. Hydraulic hysteresis was neglected in both analyses X1 and X2. In X3, the hydraulic
478 hysteretic model (HHM) was adopted for all the layers, enclosing the upper 0.10 m of the soil column.
479 Lastly, the combined effects due to the modelling of hydraulic hysteresis and the presence of the root-
480 permeated soil (A1sup) were considered in analysis X4. The soil hydraulic parameters adopted to fit
481 the MDC and the MWC were the mean values determined for each lithotype (Tables 2 and 3); the
482 curves used are shown in Figures 11b-e.
483
484 **Table 4. Summary of the numerical simulations: soil profile, hydraulic model, initial conditions and**
485 **simulation phases.**

Soil profile	Hydraulic model	Analysis	Initial conditions	Simulation phases
A1 (0.30 m) A2 (0.60 m)	MDC	X1	Hydrostatic pore water pressure distribution (s = 10 kPa at soil surface)	1) Preliminary transient simulation (1 January 2017 – 31 March 2017) ↓ 2) Simulation of hydrological year (1 April 2017-1 April 2018) ↓ 3) 48h of intense rainfall starting on 4th April 2018 and 21st March 2018
	HHM	X3		
A1sup (0.10 m) A1 (0.20 m) A2(0.60 m)	MDC	X2		
	HHM	X4		

486
487 Identical boundary conditions were applied in all the analyses. Rainfall and evapotranspiration flux
488 measured at the test site for one year (1st April 2017 – 1st April 2018) were applied at the ground
489 surface (Figure 9f) in order to investigate the soil response to seasonal meteorological cycles. Daily
490 evaporation was calculated as the potential evapotranspiration (ET_0) given by Equation 7, where T_{max}

and T_{min} are the maximum and minimum daily temperatures, respectively, and R_a is the extra-terrestrial radiation, whose variation during the year depends on the latitude of the study site[60]:

$$ET_0 = 0.0023(T_{max} + 17.8)(T_{max} - T_{min})^{0.5} R_a \quad (7)$$

The use of potential evapotranspiration over the dry period (June-October) leads to an overestimation of water outflow from the ground surface. However, no data were available to determine the actual value of evapotranspiration. The temperature measurements and variations of extra-terrestrial radiation are reported in Dias[35].

In the analyses, evapotranspiration was stopped after one year: after this phase intense rainfall, whose net intensity was equal to the saturated hydraulic conductivity of A1sup soil (the soil with the highest saturated hydraulic conductivity: $3 \times 10^{-6} m\ s^{-1}$), was imposed at the top boundary of the soil column for 48 hours. Note that, according to experience, continuous rainfall of $3 \times 10^{-6} m\ s^{-1}$(=$13\ mm\ h^{-1}$) represents an intensity sufficient to trigger flowslides in the area close to the test site. Therefore, it was used here to investigate the worst-case scenario in all carried out analyses[14,16,53,62,63]. Occurrence of water ponding was excluded, assuming that non-infiltrated water would move away as run-off. This way, the boundary condition at the ground surface consisted of a film of water (a null pore water pressure) applied during the whole duration of the heavy rainfall event.

According to Pirone et al[10], the pumice soil layer generally lying at the bottom of the modelled pyroclastic cover allows free drainage especially during the wet season (from November to May). Therefore, a free drainage condition was imposed at the bottom of the soil column.

Hydrostatic pore water pressure distribution with a maximum value of matric suction at the ground surface equal to 10 kPa was assumed as initial condition. This assumption was arbitrary; however, it was observed that a three-month simulation period is long enough to sweep out the influence of initial condition. Simplifying, meteorological conditions monitored at the test site from 1st January 2017 to 1st April 2018 were simulated in order to detect the hydrological soil response. Then, 48 hours of virtual intense rainfall were applied starting from two different profile of matric suction calculated on 4th April 2018 and on 21st March 2018. This was devoted to investigate the effect of initial matric suction on soil response to intense rainfall event (Figure 11f). A summary of the carried out numerical analyses is reported in Table 4.

5.2 Results of numerical parametric analyses

The vertical profiles of matric suction calculated by applying two days of intense rainfall starting from 4th April 2018 are reported in Figures 12a-d. The roots effect can be clearly identified by comparing Figure 12a (analysis X1) to Figure 12b (analysis X2); the wetting front moved faster when the properties of A1sup soil were assigned to the 0.10 m thick shallower layer of the soil column, taking into account the vegetation cover. Indeed, the saturated permeability of A1sup is one order of magnitude higher than that of soil A1. Positive values of pore water pressure established in the first 0.20 m of the soil column (Figure 12b) due to the permeability contrast between soils A1sup and A1. A steady state condition (no matric suction variation in time) was reached after 24 h of rainfall if soil A1sup was considered in the model (X2) and after 36 h if the root presence was disregarded (X1). To appreciate the effect of the hysteretic model (HHM), Figure 12a (X1) should be compared to Figure 12c (X3). The wetting front moved slower when the HHM was adopted even if the difference between the two models is not too big. Indeed, the water storage capacity was higher along the MWC than those determined along the MDC. While the presence of roots produced an increase in the hydraulic conductivity of the more superficial soil layer, and therefore contributed to increase the wetting front advancement rate, the higher values of the water storage capacity associated with the imbibition processes along scanning paths gave rise to a slowdown compared to what was expected considering the MDC. Lastly, the profiles obtained from the X2 analysis (Figure 12b) are very similar to those derived from X4 (Figure 12d) where both the presence of A1sup soil and hydraulic hysteresis were considered.

Matric suction, volumetric water content and hydraulic conductivity calculated during 48 h of intense rainfall at a depth of 0.50 m are plotted as a function of elapsed time in Figures 13a-c. First, matric suction predicted by analysis X1 (continuous grey line) is to be compared with X3 (dashed black line) to assess the relevance of adopting the hysteretic hydraulic model (Figure 13a). The initial value of matric suction was 1 kPa lower (15 kPa in X1, 14 kPa in X3) when the HHM is adopted. However, the model does not seem to play a major role in soil response during intense rainfall as the effects of HHM on initial conditions were cancelled during the critical event. Indeed, after 12 h, when the effects of rainfall reached the depth of 0.50 m, lower values of matric suction were predicted if water retention was modelled by the MDC (analysis X1) than if HHM was considered (X3), but after 24 h this relationship was reversed. This occurred because the steady state condition was reached later and at

lower values of matric suction when HHM was adopted. To address this issue, the paths detected at the depth of 0.50 m in the X1 and X3 analyses are shown in Figures 14a and b. The continuous grey and black lines (X3 and X1, respectively) represent paths experienced by the soil over one hydrological year (1st April 2017 to 1st April 2018), whilst the triangle and square symbols (X3 and X1, respectively) describe paths produced by the intense 48 h of rainfall. If the imbibition curve (analysis X3) was followed instead of the MDC (X1), the soil was less permeable and the steady state conditions were reached at lower values of matric suction. This presents implications on the minimal duration of rainfall that may lead to failure of an infinite slope constituted by the same stratigraphy of the soil column investigated here for which the rainwater infiltration is the main cause of instability. In fact, as it was proved by processing the field data collected at some test sites assimilable to infinite slope in Campania Region[9,49], the groundwater flow is predominantly vertical in the wet period, from November to May. Therefore, HHM is able to predict a time to failure longer or shorter than the MDC according to the duration of rainfall required to establish the critical matric suction value (i.e. the matric suction value corresponding to the safety factor of 1). If matric suction values as low as 2 kPa to 3 kPa are required to maintain slope stability, HHM would predict that the rainfall event should last at least two days to trigger a landslide. By contrast, the MDC model would never predict a failure because the steady state condition corresponds to higher matric suction values. Then, the values of matric suction calculated in X2 (dashed grey line) and X4 (continuous black line) (Figures 13a and d) are very close to one another. This highlights the important effect of the roots that partially offsets hysteresis. In any case, matric suction values predicted by considering root presence are always lower than those predicted by neglecting it, regardless of the hydraulic model adopted. Disregarding the root presence in the soil profile means overestimating matric suction values at each instant, hence overestimation of the rainfall duration required to lead to slope failure.

Matric suction, volumetric water content and hydraulic conductivity calculated at a depth of 0.5 m during a 48h rainfall event starting from 21st March 2018 are reported in Figures 13d-f. In this case, the matric suction values ranged from 5.5 kPa to 7.5 kPa before the heavy rainfall event. Also, in this case HHM (analyses X3 and X4 in Figure 13d) produced lower initial values of matric suction (the difference was about 2-3 kPa), which in turn significantly affected soil response during the subsequent intense rainfall. The matric suction predicted by HHM (X3 and X4) was always lower than those calculated with the MDC (analyses X1 and X2), regardless of rainfall duration. However, the

580 volumetric water content varied slightly among all the analyses because the soil was close to saturation
581 (Figure 1-3e). Finally, time to failure during intense rainfall in winter (matric suction value is close to
582 AEV) is overestimated if the proper hydraulic properties for rooted soil and HHM are both overlooked.
583 In this case, accounting for hydraulic hysteresis plays a major role in suitable prediction of initial
584 distribution of matric suction and volumetric water content, because the soil keeps the memory of its
585 antecedent hydraulic history also during the critical rainfall event.
586 From field experience[14,16,53,62], the rainfall event able to trigger flowslides in the monitored area
587 amounts to a maximum of 200 mm day^{-1}. Therefore, rainfall intensity of 13 mm h^{-1} (K_{sat} of the A1sup
588 layer) used in parametric analyses, with a duration lower than one day (18 h), represents a realistic
589 critical event. If 13 mm h^{-1} for less than one day occurs in spring (when matric suctions in the subsoil
590 range between 10 and 20 kPa, see Figure 11a), the use of HHM predicts higher matric suction values
591 than those predicted by the MDC, and thus false alarms could be avoided. If the same rainfall event
592 occurs in winter for initial matric suction values lower than 10 kPa along the entire soil profile, the use
593 of HHM is always recommended because the matric suctions predicted are always much lower than
594 those predicted by adopting the MDC (Figure 10d). If the hydraulic soil model does not account for
595 hysteresis, it is always strongly recommended to adopt a curve that can represent the paths exhibited by
596 the soil in the field.
597

598 ## 6 Conclusions

599 Soil hydraulic characterization greatly affects the results of physically based models used for predicting
600 flowslides. In this paper, an extensive hydraulic experimental investigation on pyroclastic soils of the
601 test site on Mt. Faito in Campania (Southern Italy) was presented. In this regard, the role of the root-
602 permeated soil and hydraulic hysteresis were analysed. The presence of roots was taken into account by
603 testing specimens collected from the upper 0.10 m of the soil profile, where the amount of biomass is
604 three times higher than that observed at greater depths. Hydraulic hysteresis was investigated by testing
605 cycles of imbibition and evaporation in a ku-pf apparatus. The hydraulic hysteretic model of Parker and
606 Lenhard[31] was adopted to fit the experimental data via inverse analysis. The parameters of the van
607 Genuchten equation for main drying and main wetting curve were then obtained. Our main findings are
608 summarized below:

- the procedure proposed by Nicotera et al[30] was extended and modified. In particular, the procedure to perform cycles of evaporation and imbibition in the ku-pf apparatus was presented in order to allow successful calibration of the Parker & Lenhard[31] hysteretic hydraulic model through inverse analysis using the software HYDRUS-1D;
- the mean values of the main drying parameters of the Mualem-van Genuchten model were in good agreement with those found for pyroclastic soils sampled in test sites in the same regional context. All the investigated soils behaved like coarse-grained materials as the AEV ranged from 2 kPa to 8 kPa, apart from soil layer C2. The measurements of saturated permeability varied two orders of magnitude along the vertical profile ranging from $1 \times 10^{-7} m\, s^{-1}$ to $1 \times 10^{-5} m\, s^{-1}$. In particular, the saturated permeability determined on the specimens collected in the top 0.10 m (soil A1sup) was one order of magnitude higher than that estimated on specimens collected at 0.60 m of depth (soil A1).
- the hysteretic model only required two additional parameters (α^w and θ_s^w) in comparison to a single curve model. The values of both parameters could be expressed in relation to those determined along the drying curve: θ_s^w varied between 0.84 and 1.00 θ_s^d, indicating the fraction of entrapped air in the soil pores; α^w varied on average between 1.01 and 3.97 (on average 1.72 and 2.97) α^d. Therefore, in the absence of experimental data providing the hysteretic loops, assigning α^w equal to $2\alpha^d$ and θ_s^w equal to $0.90\,\theta_s^d$ were reasonable assumptions.
- the dry root biomass, M_{root}, is correlated to hydraulic saturated conductivity: the soil specimen with more roots show a higher hydraulic saturated conductivity. This behaviour has been associated to preferential flow induced by drying and wetting cycles experienced during plant growth. In the top layer A, the M_{root} also affects the θ_s^d and the AEV of WRC. The θ_s^d increases with the root biomass because of production of the root exudation. Lastly, the AEV decreases with the increase of M_{root}, due to formation of soil lumps and micro-cracks would desaturate at a lower matric suction than the soil sample without.

The effects of hydraulic properties of root-permeated soil and hysteretic hydraulic models on the simulation of the soil response to intense rainfall events were investigated through parametric analyses. Two soil columns differentiated by the presence of roots in the shallower 0.10 m of soil were considered in the analyses. The importance of the hydraulic model was also investigated by comparing

results obtained by representing the WRC with the main drying curve or with a hysteretic model. The main findings of the numerical investigation were:

- The use of the proper hydraulic characterization for the first centimetres of the soil column is essential to simulate the presence of roots properly because this soil layer regulates rainwater infiltration at the ground surface;
- The use of HHM affects: (i) estimation of the initial distribution of matric suction and volumetric water content before the simulation of a critical rainfall event; and (ii) the soil response to intense rainfall. The first effect prevails largely over the second during the wet period (October to February) when initial matric suction is lower than 10 kPa.

Acknowledgments

The authors wish to acknowledge the support of the European Commission via the Marie Skłodowska-Curie Innovative Training Networks (ITN-ETN) project TERRE 'Training Engineers and Researchers to Rethink geotechnical Engineering for a low carbon future' (H2020-MSCA-ITN-2015-675762).

References

1. Li WC, Dai FC, Wei YQ, Wang ML, Min H, Lee LM. Implication of subsurface flow on rainfall-induced landslide: a case study. *Landslides*. 2016;13(5):1109-1123. doi:10.1007/s10346-015-0619-9
2. Ietto F, Perri F, Cella F. Geotechnical and landslide aspects in weathered granitoid rock masses (Serre Massif, southern Calabria, Italy). *Catena*. 2016;145:301-315. doi:10.1016/j.catena.2016.06.027
3. Mikoš M, Petkovšek A, Majes B. Mechanisms of landslides in over-consolidated clays and flysch: Activity scale and targeted region: National. *Landslides*. 2009;6(4):367-371. doi:10.1007/s10346-009-0171-6
4. Pánek T, Hradecký J, Minár J, Šilhán K. Recurrent landslides predisposed by fault-induced weathering of flysch in the Western Carpathians. *Geol Soc Eng Geol Spec Publ*. 2010;23:183-199. doi:10.1144/EGSP23.11
5. Calcaterra D, De Riso R, Evangelista A, Nicotera M V, Santo A, Scotto di Santolo A. Slope instabilities in the pyroclastic deposits of the Phlegraean district and the carbonate Apennine

669 (Campania, Italy). In: Picarelli L, ed. *International Workshop on Occurrence and Mechanisms*
670 *of Flows in Natural Slopes and Earthfills*. Patron, Bologna; 2003:61-76.
671 6. Picarelli L, Olivares L, Comegna L, Damiano E. Mechanical aspects of flow-like movements
672 in granular and fine grained soils. *Rock Mech Rock Eng*. 2008;41(1):179-197.
673 doi:10.1007/s00603-007-0135-x
674 7. Sorbino G, Nicotera MV. Unsaturated soil mechanics in rainfall-induced flow landslides. *Eng*
675 *Geol*. 2013;165:105-132. doi:10.1016/J.ENGGEO.2012.10.008
676 8. Cascini L, Sorbino G, Cuomo S, Ferlisi S. Seasonal effects of rainfall on the shallow
677 pyroclastic deposits of the Campania region (southern Italy). *Landslides*. 2014;11(5):779-792.
678 doi:10.1007/s10346-013-0395-3
679 9. Pirone M, Papa R, Nicotera MV, Urciuoli G. In situ monitoring of the groundwater field in an
680 unsaturated pyroclastic slope for slope stability evaluation. *Landslides*. 2015;12(2):259-276.
681 doi:10.1007/s10346-014-0483-z
682 10. Pirone M, Papa R, Nicotera MV, Urciuoli G. Soil water balance in an unsaturated pyroclastic
683 slope for evaluation of soil hydraulic behaviour and boundary conditions. *J Hydrol*.
684 2015;528:63-83. doi:10.1016/j.jhydrol.2015.06.005
685 11. Pirone M, Urciuoli G. Cyclical suction characteristics in unsaturated slopes. In: *Volcanic*
686 *Rocks and Soils - Proceedings of the International Workshop on Volcanic Rocks and Soils,*
687 *2015*. ; 2015:183-184. doi:10.1201/b18897-53
688 12. Pirone M, Papa R, Nicotera MV, Urciuoli G. Hydro-mechanical analysis of an unsaturated
689 pyroclastic slope based on monitoring data. In: Lollino, G., Giordan, D., Crosta, G.,
690 Corominas, J., Azzam, R., Wasowski, J., Sciarra N, ed. *Engineering Geology for Society and*
691 *Territory - Volume 2: Landslide Processes*. Springer International Publishing; 2015:1069-
692 1073. doi:10.1007/978-3-319-09057-3_189
693 13. Comegna L, Rianna G, Lee SG, Picarelli L. Influence of the wetting path on the mechanical
694 response of shallow unsaturated sloping covers. *Comput Geotech*. 2016;73:164-169.
695 doi:10.1016/j.compgeo.2015.11.026
696 14. Santo A, Di Crescenzo G, Forte G, Papa R, Pirone M, Urciuoli G. Flow-type landslides in
697 pyroclastic soils on flysch bedrock in southern Italy: the Bosco de' Preti case study.
698 *Landslides*. 2018;15(1):63-82. doi:10.1007/s10346-017-0854-3

15. Balzano B, Tarantino A, Nicotera MV, Forte G, de Falco M, Santo A. Building physically based models for assessing rainfall-induced shallow landslide hazard at catchment scale: Case study of the Sorrento Peninsula (Italy). *Can Geotech J*. 2019;56(9):1291-1303. doi:10.1139/cgj-2017-0611
16. Forte G, Pirone M, Santo A, Nicotera MV, Urciuoli G. Triggering and predisposing factors for flow-like landslides in pyroclastic soils: the case study of the Lattari Mts. (southern Italy). *Eng Geol*. 2019;257:105137. doi:10.1016/j.enggeo.2019.05.014
17. Di Maio R, De Paola C, Forte G, et al. An integrated geological, geotechnical and geophysical approach to identify predisposing factors for flowslide occurrence. *Eng Geol*. 2020;267. doi:10.1016/j.enggeo.2019.105473
18. Pagano L, Reder A, Rianna G. Effects of vegetation on hydrological response of silty volcanic covers. *Can Geotech J*. 2019;56(9):1261-1277. doi:10.1139/cgj-2017-0625
19. Bashir R, Sharma J, Stefaniak H. Effect of hysteresis of soil-water characteristic curves on infiltration under different climatic conditions. *Can Geotech J*. 2016;53(2):273-284. doi:10.1139/cgj-2015-0004
20. Rianna G, Comegna L, Pagano L, Picarelli L, Reder A. The role of hydraulic hysteresis on the hydrological response of pyroclastic silty covers. *Water (Switzerland)*. 2019;11(3). doi:10.3390/w11030628
21. Angers DA, Caron J. Plant-induces changes in soil structure: Processes and feedbacks. *Biogeochemistry*. 1998;42(1/2):55-72. doi:10.1023/A:1005944025343
22. Leung AK, Garg A, Ng CWW. Effects of plant roots on soil-water retention and induced suction in vegetated soil. *Eng Geol*. 2015;193:183-197. doi:10.1016/j.enggeo.2015.04.017
23. Ng CWW, Leung AK, Woon KX. Effects of soil density on grass-induced suction distributions in compacted soil subjected to rainfall. *Can Geotech J*. 2014;51(3):311-321. doi:10.1139/cgj-2013-0221
24. Ng CWW, Ni JJ, Leung AK, Wang ZJ. A new and simple water retention model for root-permeated soils. *Géotechnique Lett*. 2016;6:1-6. doi:10.1680/jgele.15.00187
25. Ni JJ, Leung AK, Ng CWW, Shao W. Modelling hydro-mechanical reinforcements of plants to slope stability. *Comput Geotech*. 2018;95:99-109. doi:10.1016/j.compgeo.2017.09.001

728 26. Ni J-J, Cheng Y-F, Bordoloi S, et al. Investigating plant root effects on soil electrical
729 conductivity: An integrated field monitoring and statistical modelling approach. 2018.
730 doi:10.1002/esp.4533
731 27. Leung, A. K., Boldrin, D., Liang, T., Wu, Z. Y., Kamchoom, V., & Bengough, A. G. 2018.
732 Plant age effects on soil infiltration rate during early plant establishment, 68(7): 646 - 652.
733 28. Song, L., Li, J. H., Zhou, T. & Fredlund, D. G. (2017). Experimental study on unsaturated
734 hydraulic properties of vegetated soil. Ecol. Engng 103, Part A, 207-216.7
735 29. Jotisankasa, A. & Sirirattanachat, T. (2017). Effects of grass roots on soil-water retention
736 curve and permeability function. Can. Geotech. J 54, No. 11, 1612-1622.
737 30. Nicotera MV, Papa R, Urciuoli G. An experimental technique for determining the hydraulic
738 properties of unsaturated pyroclastic soils. *Geotech Test J*. 2010;33(4):263-285.
739 doi:10.1520/GTJ102769
740 31. Parker JC, Lenhard RJ. A model for hysteretic constitutive relations governing multiphase
741 flow: 1. Saturation-pressure relations. *Water Resour Res*. 1987;23(12):2187-2196.
742 doi:10.1029/WR023i012p02187
743 32. Di Crescenzo G, Santo A. Debris slides-rapid earth flows in the carbonate massifs of the
744 Campania region (Southern Italy): Morphological and morphometric data for evaluating
745 triggering susceptibility. *Geomorphology*. 2005;66:255-276.
746 doi:10.1016/j.geomorph.2004.09.015
747 33. ASTM D2487-17, Standard Practice for Classification of Soils for Engineering Purposes
748 (Unified Soil Classification System), ASTM International, West Conshohocken, PA, 2017.
749 www.astm.org
750 34. ASTM D854-14, Standard Test Methods for Specific Gravity of Soil Solids by Water
751 Pycnometer, ASTM International, West Conshohocken, PA, 2014, www.astm.org
752 35. Dias ASRA. The effect of vegetation on slope stability of shallow pyroclastic soil covers.
753 [PhD thesis], Naples, University of Naples Federico II, University of Montpellier, 2019.
754 https://tel.archives-ouvertes.fr/tel-02045922
755 36. Simpson W, TenWolde A. Physical properties and moisture relations of wood. *Wood Handb*
756 *wood as an Eng Mater*. 1999:3.1-3.24. doi:10.1007/s13398-014-0173-7.2

37. Vanapalli SK, Fredlund DG, Pufahl DE. The influence of soil structure and stress history on the soil-water characteristic of a compacted. *Geotechnique*. 1999;49(9):143-159. doi:10.3906/zoo-0809-14
38. Nicotera MV, Papa R, Urciuoli G. The Hydro-Mechanical Behaviour of Unsaturated Pyroclastic Soils: An Experimental Investigation. *Eng. Geol*. 2015; 195, 70–84
39. Papa R. Indagine Sperimentale sulla Coltre Piroclastica di un Versante della Campania [Experimental investigation on the pyroclastic cover of a slope in Campania (Italy)]. Ph.D. Thesis, Università di Napoli Federico II, Napoli, Italy, 2007; p. 367.
40. Lenhard RJ, Parker JC, Kaluarachchi JJ. Comparing Simulated and Experimental Hysteretic Two-Phase Transient Fluid Flow Phenomena. *Water Resour Res*. 1991;27(8):2113-2124. doi:10.1029/91WR01272
41. Šimůnek J, Šejna M, Saito H, Sakai M, van Genuchten MT. The HYDRUS-1D Software Package for Simulating the One-Dimensional Movement of Water, Heat, and Multiple Solutes in Variably-Saturated Media. Version 4.17, 2013
42. van Genuchten MT. A Closed-form Equation for Predicting the Hydraulic Conductivity of Unsaturated Soils. *Soil Sci Soc Am J*. 1980;44(5):892-898. doi:10.2136/sssaj1980.03615995004400050002x
43. Vogel T, Huang K, Zhang R, van Genuchten MT. *The HYDRUS Code for Simulating One-Dimensional Water Flow, Solute Transport, and Heat Movement in Variably-Saturated Media. Version 5.0*. Riverside, California; 1996. doi:10.13140/RG.2.1.3456.7525
44. Mualem Y. A new model for predicting the hydraulic conductivity of unsaturated porous media. *Water Resour Res*. 1976;12(3):513-522. doi:10.1029/WR012i003p00513
45. Tarantola A. Inverse problem theory and methods for model parameter estimation. Vol. 89, siam., 2005.
46. Marquardt DW. An Algorithm for Least-Squares Estimation of Nonlinear Parameters. *J Soc Ind Appl Math*. 1963;11(2):431-441. doi:10.1137/0111030
47. Kool JB, Parker JC. Development and evaluation of closed-form expressions for hysteretic soil hydraulic properties. *Water Resour Res*. 1987;23(1):105-114. doi:10.1029/WR023i001p00105

48. Freeze RA. The Mechanism of Natural Ground-Water Recharge and Discharge: 1. One-dimensional, Vertical, Unsteady, Unsaturated Flow above a Recharging or Discharging Ground-Water Flow System. *Water Resour Res*. 1969;5(1):153-171. doi:10.1029/WR005i001p00153
49. Damiano E, Olivares L, Picarelli L. Steep-slope monitoring in unsaturated pyroclastic soils. *Eng Geol*. 2012;137-138:1-12. doi:10.1016/j.enggeo.2012.03.002
50. Soltani A, Azimi M, Deng A, Taheri A. A simplified method for determination of the soil–water characteristic curve variables. *Int J Geotech Eng*. 2019;13(4):316-325. doi:10.1080/19386362.2017.1344450
51. Hillel D. *Fundamentals of Soil Physics*.; 2013. doi:10.1016/C2009-0-03109-2
52. Basile A, Ciollaro G, Coppola A. Hysteresis in soil water characteristics as a key to interpreting comparisons of laboratory and field measured hydraulic properties. *Water Resour Res*. 2003;39(12):1355. doi:10.1029/2003WR002432
53. Pirone M, Papa R, Nicotera MV, Urciuoli G. Hydraulic Behaviour of Unsaturated Pyroclastic Soil Observed at Different Scales. In: *Procedia Engineering*. Vol 158; 2016:182-187. doi:10.1016/j.proeng.2016.08.426
54. Lu N, Alsherif N, Wayllace A, and Godt J. Closing the Loop of the Soil Water Retention Curve. *Journal of Geotechnical and Geoenvironmental Engineering* 2014; 141(1): 1. doi:10.1061/(ASCE)GT.1943-5606.0001225.
55. Tarantino A, Tombolato S. Coupling of hydraulic and mechanical behaviour in unsaturated compacted clay. *Geotechnique* 2005; 55 (4): 307-317. doi: 10.1680/geot.2005.55.4.307
56. Gallipoli D. A hysteretic soil-water retention model accounting for cyclic variations of suction and void ratio. *Geotechnique* 2012; 62(7): 605-616
57. Li JH, Li L, Chen R, Li DQ. Cracking and vertical preferential flow through landfill clay liners. *Engineering Geology* 2016; 206: 33-41. doi:10.1016/j.enggeo.2016.03.006.
58. Vergani C, Graf F. Soil permeability, aggregate stability and root growth: a pot experiment from a soil bioengineering perspective. *Ecohydrology*. 2016; 9(5): 830-842. doi:10.1002/eco.1686

59. Rahardjo H, Satyanaga A, Leong EC, Santoso VA, Ng YS. Performance of an Instrumented Slope Covered with Shrubs and Deep Rooted Grass. *Soils and Foundations.* 2014; 54(3): 417-425. doi: 10.1016/j.sandf.2014.04.010.
60. Fredlund DG, Rahardjo H, Fredlund MD. *Unsaturated Soil Mechanics in Engineering Practice*.; 2012. doi:10.1002/9781118280492
61. Allen RG, Pereira LS, Raes D, Smith M. *Crop Evapotranspiration: Guidelines for Computing Crop Water Requirements*. FAO Irriga.; 1998. doi:10.1016/j.eja.2010.12.001
62. Pirone M, Papa R, Nicotera M V., Urciuoli G. Analysis of Safety Factor in unsaturated pyroclastic slope. In: *Landslides and Engineered Slopes. Experience, Theory and Practice*. Vol 3. Naples, Italy: CRC Press; 2016:1647-1654. doi:10.1201/b21520-204
63. Urciuoli, G., Pirone, M., Comegna, L., Picarelli, L. Long-term investigations on the pore pressure regime in saturated and unsaturated sloping soils. *Eng. Geol.* 2016 , 212: 98–119.

List of figures

Figure 1. Location of the test site on the Lattari Mts. (a); mean stratigraphic profile (b) and photos of the layers observed in trenches (c-e); grain size distribution of each soil layer (f-i).

Figure 2. Ku-pf apparatus overview (a), detail of the basket (b) and soil sample (c).

Figure 3. Negative logarithm of the saturated permeability (a), root dry biomass (b), fraction of silt in terms of mass (c), and porosity of bare soil (d) of each lithotype (the boxes contain the second and third quartile, the horizontal line inside the box is the median, "x" represents the average value, and the whiskers represent the minimum and maximum values excluding outliers).

Figure 4. Experimental measurements of matric suction at top and bottom tensiometers (s top and s bot, respectively) and volumetric water content (vwc, θ) over time (a) and zoom of a wetting step (b) carried out on sample 1.4.1 (soil A2).

Figure 5. Experimental data and simulations correspondent to sample 1.4.1 (soil A2) presented as an example. Main drying (black continuous line) and main wetting branch (black dotted line) of the WRC determined by inverse analyses, and parameters used for fitting (AEV and PP) with the drying and wetting cycles determined experimentally (dry 1, wet 1, dry 2, wet 2, dry 3) (a). The main drying (black continuous line) and wetting HPF (black dotted line) hydraulic conductivity, and measured saturated hydraulic conductivity (K_{sat}) (b). Measured cycles and the main drying and main drying branches (close up of a) compared to the model simulations (c). Comparison of the back-analysed matric suction and the average of the measured experimental values (d).

Figure 6. Mualem-van Genuchten model parameters of MDCs (a-e) and of MWCs (f, g) (the boxes contain the second and third quartile, the horizontal line inside the box is the median, the "x" represents the average value, and the whiskers represent the minimum and maximum values excluding outliers).

Figure 7. Main drying and wetting branches of the WRC (a-e) and main drying and wetting branches of the HCF (f-j) obtained for each soil type: A1sup (a, f), A1 (b, g), A2 (c, h), C1 (d, i), C2 (e, j).

Figure 8. Trellis plot: Mualem-van Genuchten model parameters of main drying and wetting branch plotted against each other.

Figure 9. Trellis plot: Root Dry biomass, M_{root}, soil porosity, n, saturated hydraulic conductivity, K_{sat}, saturated volumetric water content, θ_s^d, air entry value, AEV, plotted against each other.

Figure 10. Water storage capacity of each soil layer computed with the mean fitting parameters of the main drying (a) and wetting (b) branches of the WRCs.

857 **Figure 11.** Soil column (a), WRCs (b, c) and HCFs (d, e), and upper boundary conditions (f) modelled
858 in the numerical simulations.
859 **Figure 12. Matric** suction profile determined in X1 (a), X2 (c), X3 (b) and X4 (d) analyses at different
860 instants after the initiation of the intense rainfall.
861 **Figure 13.** Matric suction (a), volumetric water content (b) and hydraulic conductivity (c) determined
862 at the depth of 0.50 m during 48 h of intense rainfall considering the initial condition determined on 4th
863 April 2018. Matric suction (d), volumetric water content (e) and hydraulic conductivity (f) determined
864 at the depth of 0.50 m during 48 h of intense rainfall considering the initial condition determined on
865 21st March 2018.
866 **Figure 14.** Paths estimated over one year, from 1st January 2017 to 1st April 2018 (continuous lines), in
867 soil profiles without roots (without soil A1sup) differentiating between the analysis X1 (MDC, black
868 line) and analysis X3 (HHM, grey line). The paths estimated during 48 h intense rainfall (triangle
869 symbols for analysis X1; square symbols for analysis X3).
870

List of tables

Table 1. Soil physical properties and root information of each tested specimen: sampling depth (z), soil particle specific gravity (G_s), soil dry density not accounting for the presence of roots (γ_d), soil porosity of bare soil (n_0), root dry biomass (M_{roots}), root volume ratio (R_v), and root-permeated soil porosity (n).

Table 2. Values of Mualem–van Genuchten model parameters derived via inverse analysis of the first drying phase.

Table 3. Values of Mualem–van Genuchten model parameters of the main wetting curve derived via inverse analysis.

Table 4. Summary of the numerical simulations: soil profile, hydraulic model, initial conditions and simulation phases.

882 **List of symbols**

AEV	Air-entry value
C	Water storage capacity
ET_0	Potential evapotranspiration
G_s	Soil specific gravity
HHM	Hydraulic hysteretic model
HCF	Hydraulic conductivity function
K	Soil hydraulic conductivity
K-P-S	Hydraulic conductivity – pore Pressure – Saturation
K_s	Actual saturated permeability
K_{sat}	Saturated hydraulic conductivity
K_{sat}^{d}	Saturated hydraulic conductivity of the drying branch
K_{sat}^{w}	Saturated hydraulic conductivity of the wetting branch
l	Fitting parameter of the HCF
m	Fitting parameter of the K-P-S model
MDC	Main drying curve
M_{roots}	Root dry biomass in each soil specimen
MWC	Main wetting curve
n_v	Fitting parameter of the van Genuchten equation
n_0	Soil porosity ignoring the presence of roots
n	Root-permeated soil porosity
PP	Data point (θ,s) obtained from the measurements performed in the pressure plate
R_v	Root volume ratio
R_a	Extraterrestrial radiation
R^2	Coefficient of determination
S	Effective saturation
s	Matric suction
T_{max}	Maximum daily temperature
T_{min}	Minimum daily temperature

WRC	Water retention curve
z	Depth
α	Fitting parameter of the van Genuchten equation (in the main wetting or main drying)
α^d	Fitting parameter of the van Genuchten equation of the drying branch
α^w	Fitting parameter of the van Genuchten equation of the wetting branch
γ_d	Soil dry density
θ	Volumetric water content
θ_r	Residual volumetric water content
θ_s	Volumetric water content at saturation (in the main wetting or main drying)
θ_s^d	Volumetric water content at saturation of the drying branch
θ_s^w	Volumetric water content at saturation of the wetting branch

883

884

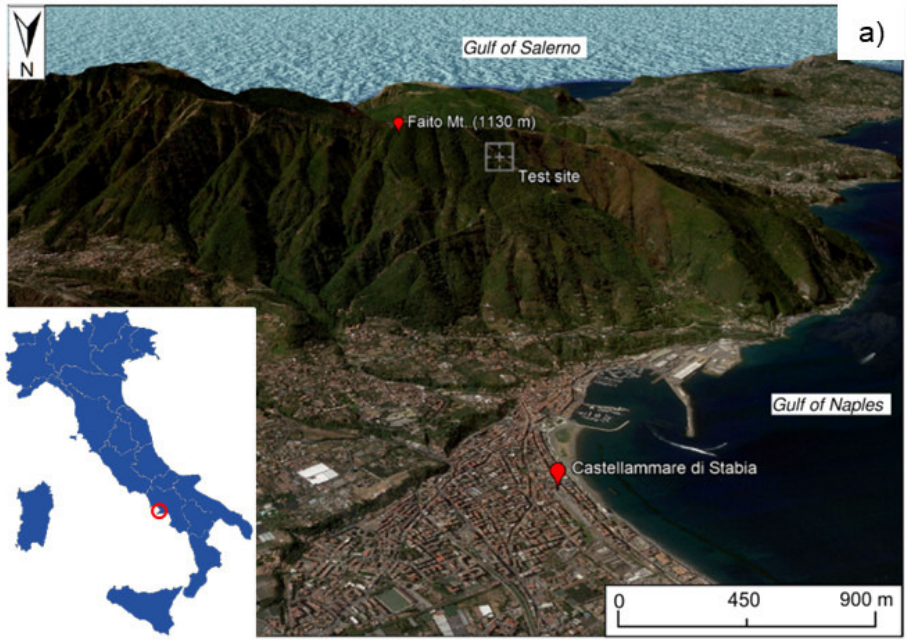
a)
N
Gulf of Salerno
Faito Mt. (1130 m)
Test site
Gulf of Naples
Castellammare di Stabia
0
450
900 m

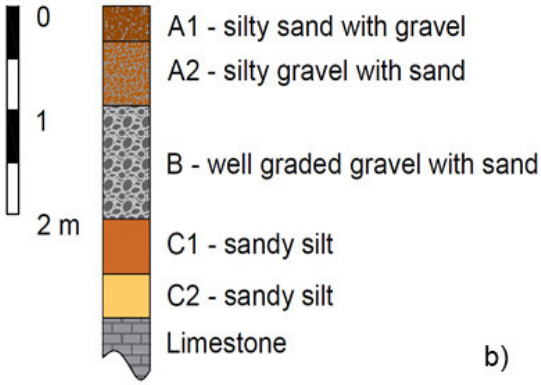
0
1
2 m
A1 - silty sand with gravel
A2 - silty gravel with sand
B - well graded gravel with sand
C1 - sandy silt
C2 - sandy silt
Limestone
b)

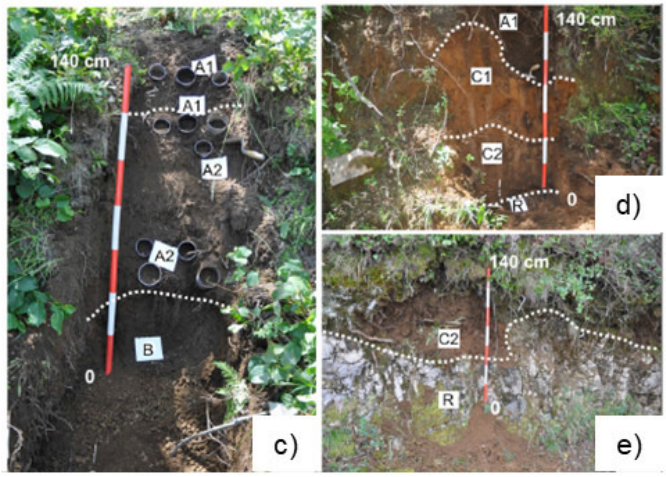
140 cm
A1
A1
A2
A2
B
0
c)
A1
140 cm
C1
C2
R
0
d)
140 cm
C2
R
0
e)

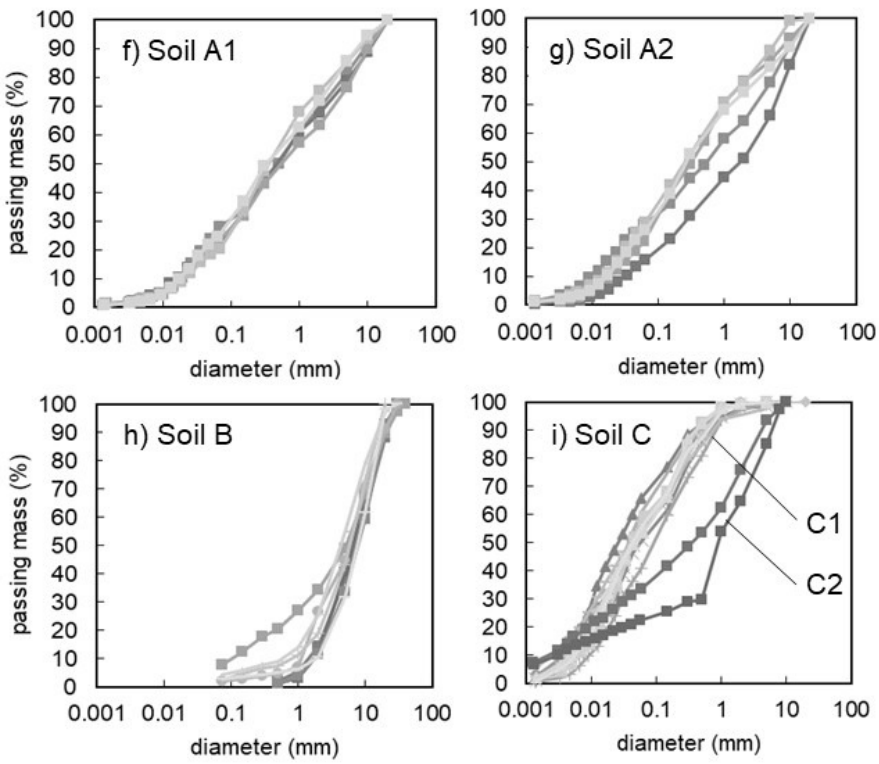
f) Soil A1
g) Soil A2
h) Soil B
i) Soil C
C1
C2
passing mass (%)
diameter (mm)
0.001
0.01
0.1
1
10
100

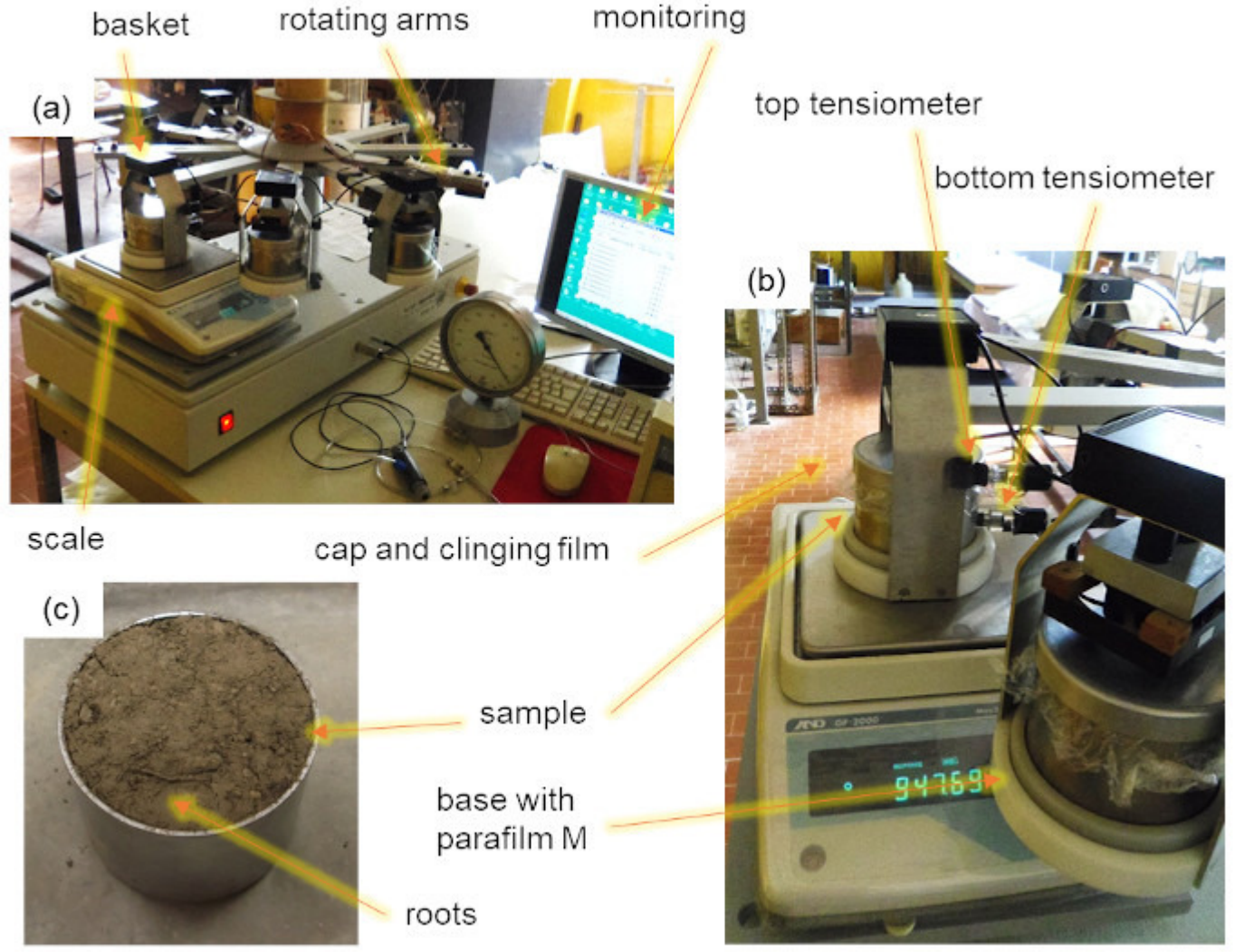
basket
rotating arms
monitoring
(a)
top tensiometer
bottom tensiometer
(b)
scale
cap and clinging film
(c)
sample
base with
parafilm M
roots

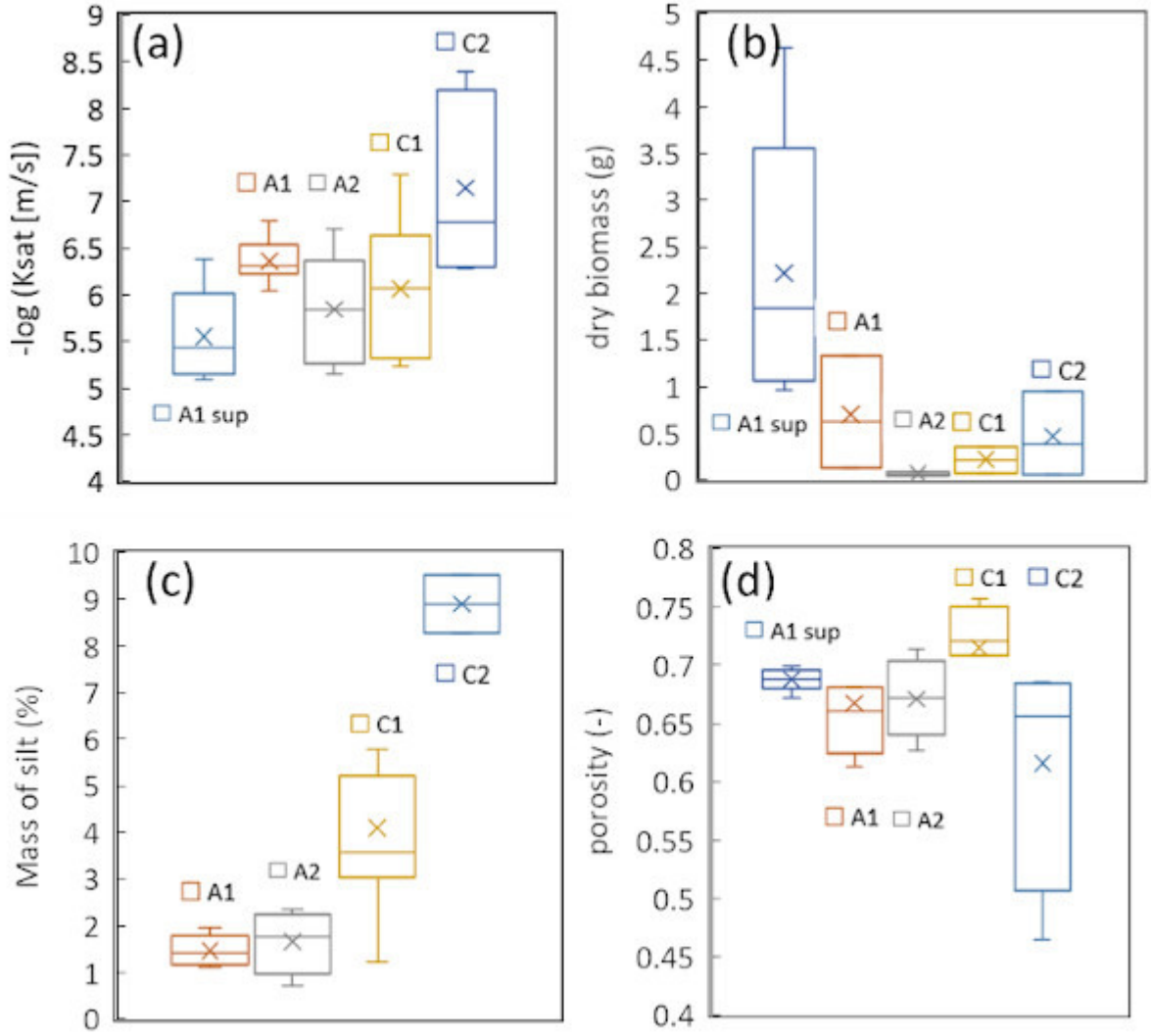
(a)
-log (Ksat [m/s])
9
8.5
8
7.5
7
6.5
6
5.5
5
4.5
4
A1 sup
A1
A2
C1
C2
(b)
dry biomass (g)
5
4.5
4
3.5
3
2.5
2
1.5
1
0.5
0
A1 sup
A1
A2
C1
C2
(c)
Mass of silt (%)
10
9
8
7
6
5
4
3
2
1
0
A1
A2
C1
C2
(d)
porosity (-)
0.8
0.75
0.7
0.65
0.6
0.55
0.5
0.45
0.4
A1 sup
A1
A2
C1
C2

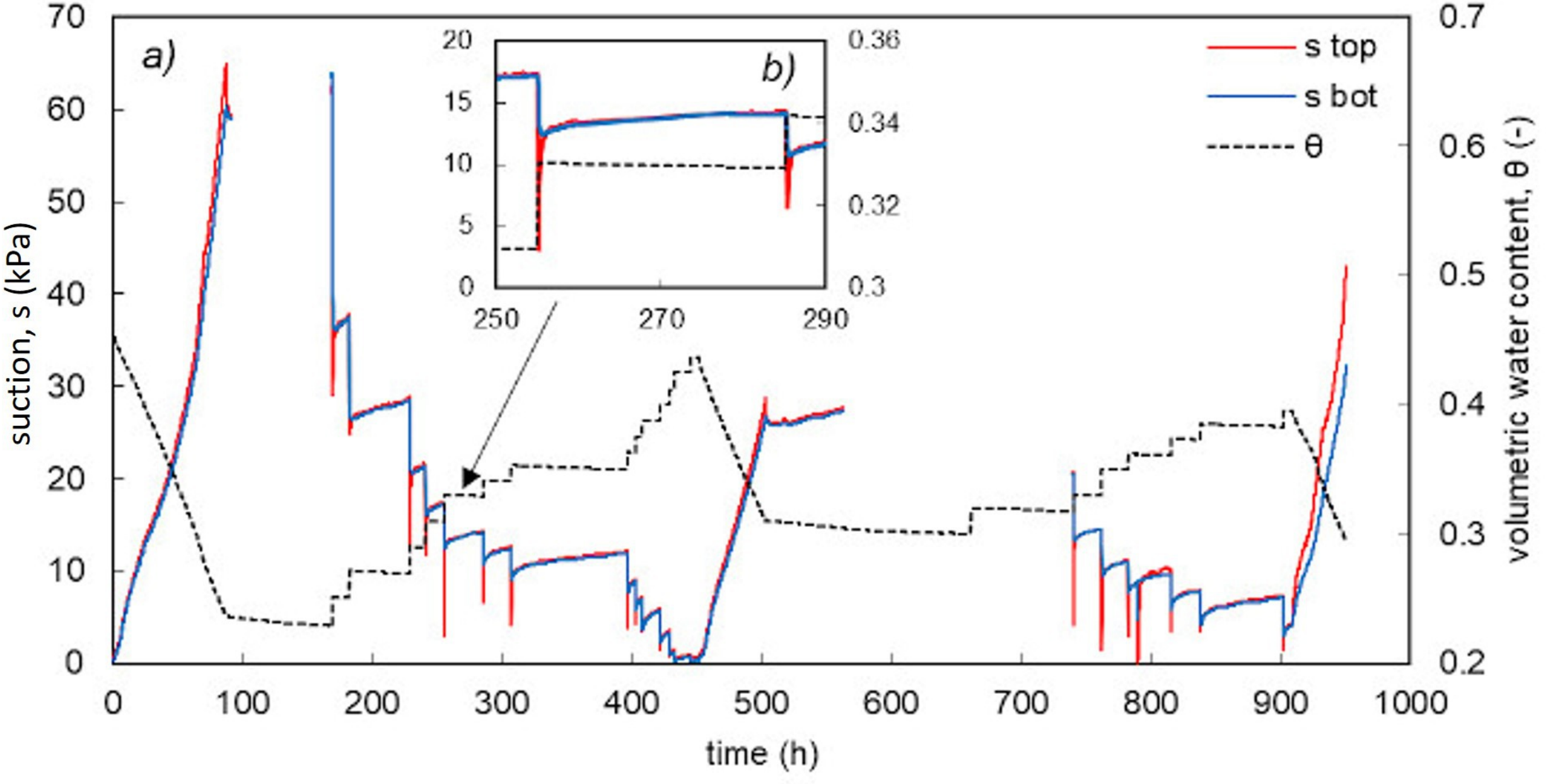
a)
b)
s top
s bot
θ
suction, s (kPa)
volumetric water content, θ (-)
time (h)
0
10
20
30
40
50
60
70
0.2
0.3
0.4
0.5
0.6
0.7
0
100
200
300
400
500
600
700
800
900
1000
0
5
10
15
20
0.3
0.32
0.34
0.36
250
270
290

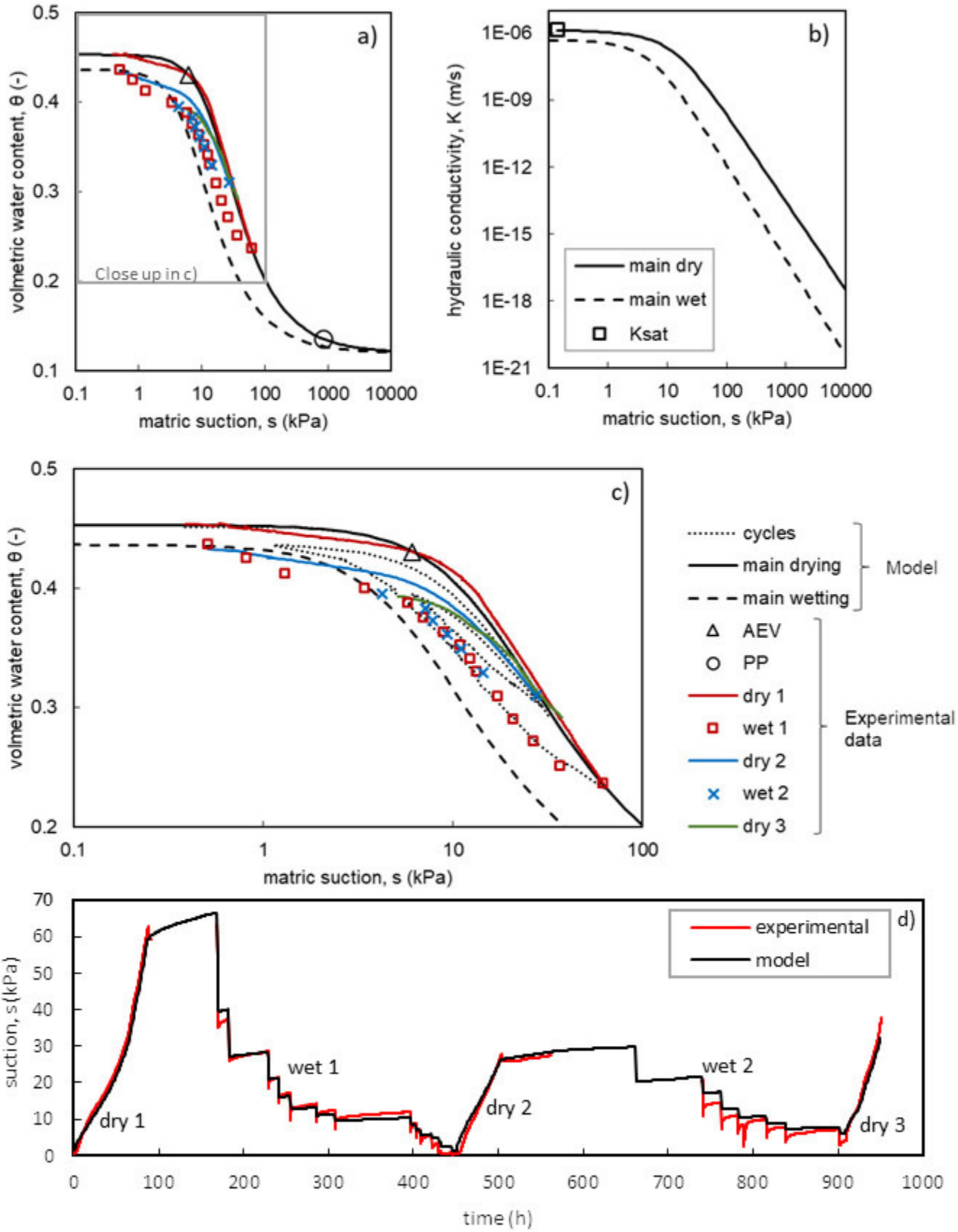
a)
volmetric water content, θ (-)
0.5
0.4
0.3
0.2
0.1
Close up in c)
0.1
1
10
100
1000
10000
matric suction, s (kPa)
b)
hydraulic conductivity, K (m/s)
1E-06
1E-09
1E-12
1E-15
1E-18
1E-21
main dry
main wet
Ksat
matric suction, s (kPa)
c)
volmetric water content, θ (-)
matric suction, s (kPa)
cycles
main drying
main wetting
Model
AEV
PP
dry 1
wet 1
dry 2
wet 2
dry 3
Experimental data
d)
experimental
model
suction, s (kPa)
dry 1
wet 1
dry 2
wet 2
dry 3
time (h)

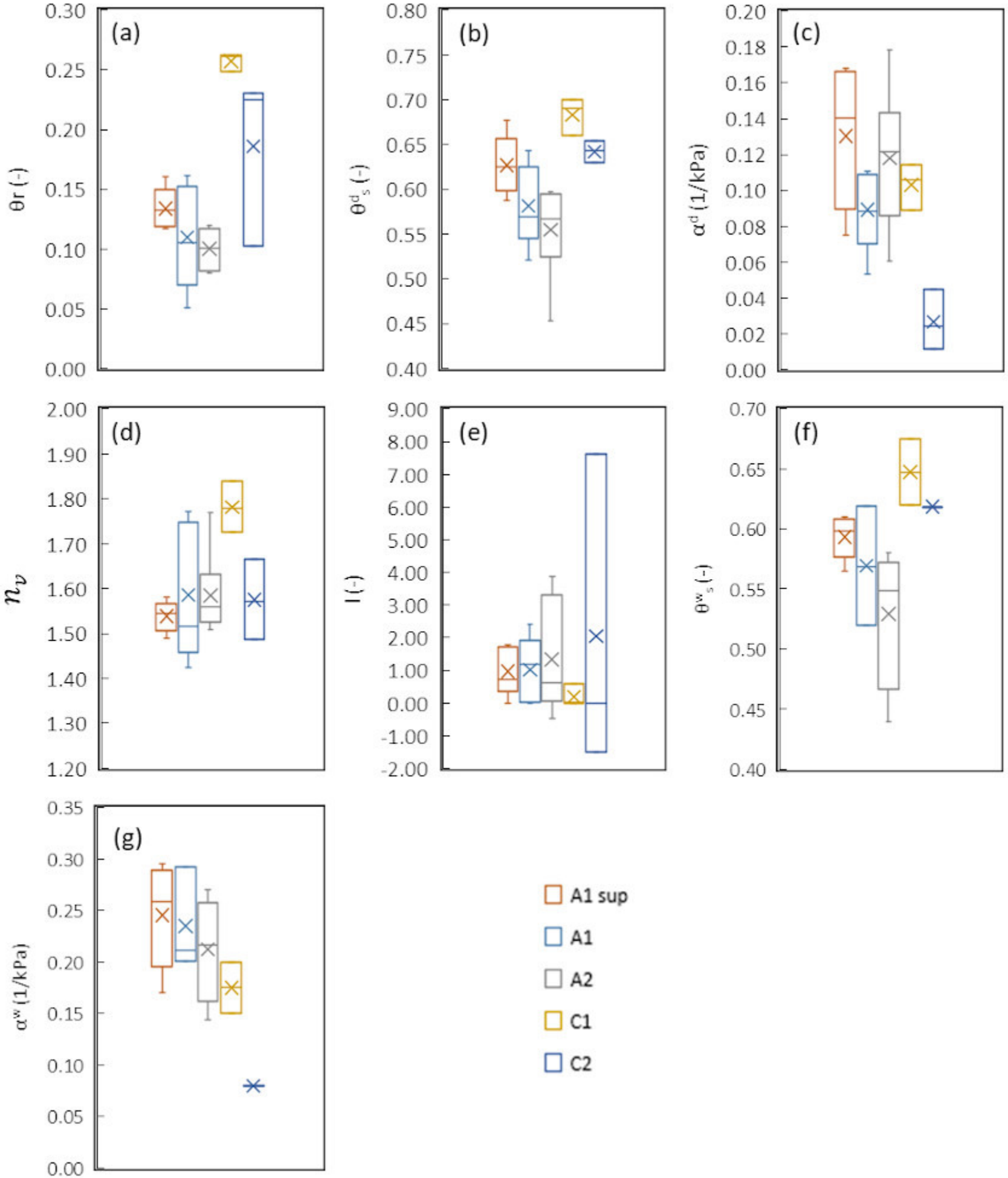
(a)
θr (-)
0.30
0.25
0.20
0.15
0.10
0.05
0.00
(b)
θ$^{d}_{s}$ (-)
0.80
0.75
0.70
0.65
0.60
0.55
0.50
0.45
0.40
(c)
α^{d} (1/kPa)
0.20
0.18
0.16
0.14
0.12
0.10
0.08
0.06
0.04
0.02
0.00
(d)
η_v
2.00
1.90
1.80
1.70
1.60
1.50
1.40
1.30
1.20
(e)
I (-)
9.00
8.00
7.00
6.00
5.00
4.00
3.00
2.00
1.00
0.00
-1.00
-2.00
(f)
θ$^{w}_{s}$ (-)
0.70
0.65
0.60
0.55
0.50
0.45
0.40
(g)
α^{w} (1/kPa)
0.35
0.30
0.25
0.20
0.15
0.10
0.05
0.00
A1 sup
A1
A2
C1
C2

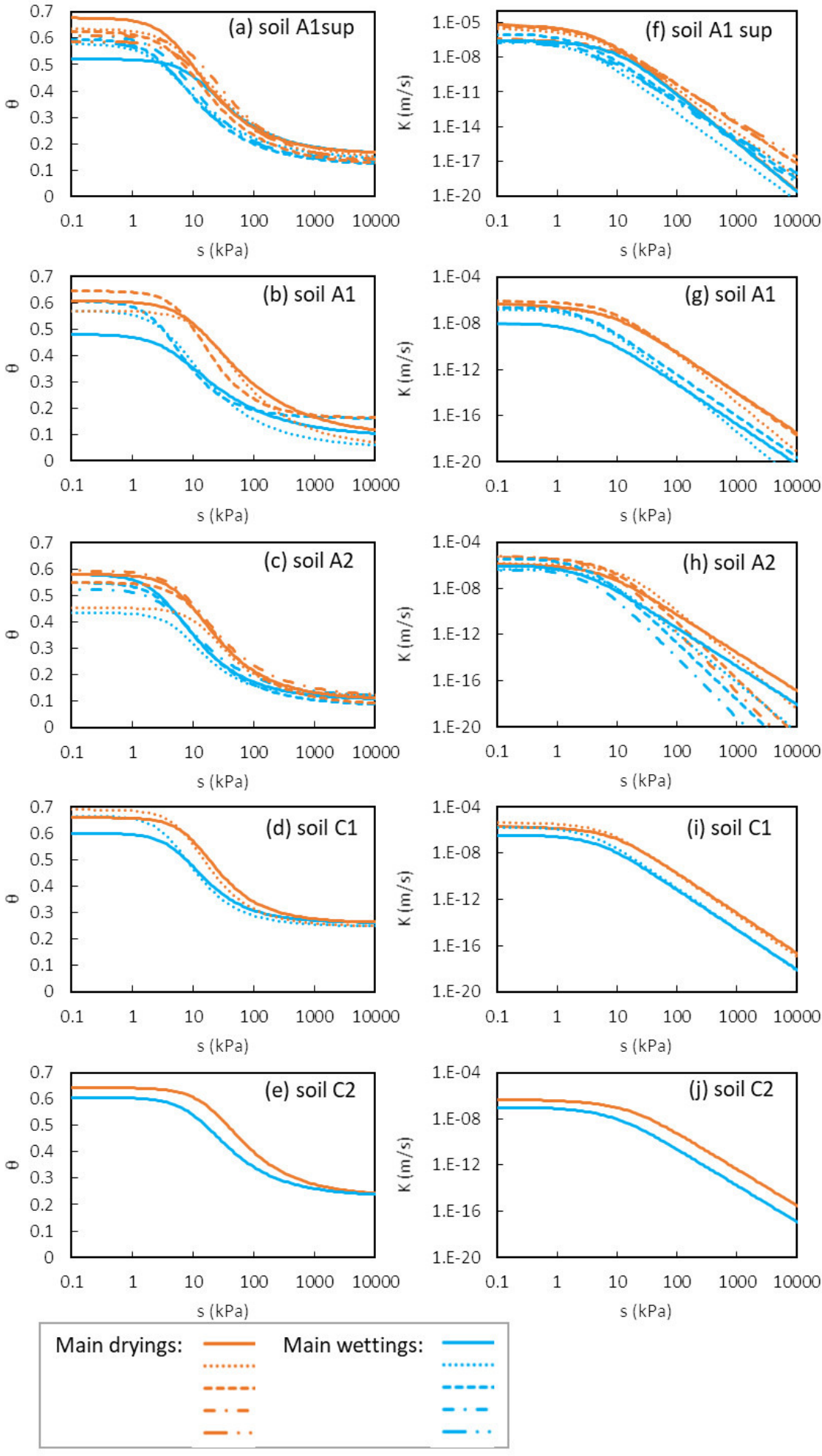
(a) soil A1sup
(f) soil A1 sup
(b) soil A1
(g) soil A1
(c) soil A2
(h) soil A2
(d) soil C1
(i) soil C1
(e) soil C2
(j) soil C2
θ
K (m/s)
s (kPa)
0.1
1
10
100
1000
10000
Main dryings:
Main wettings:

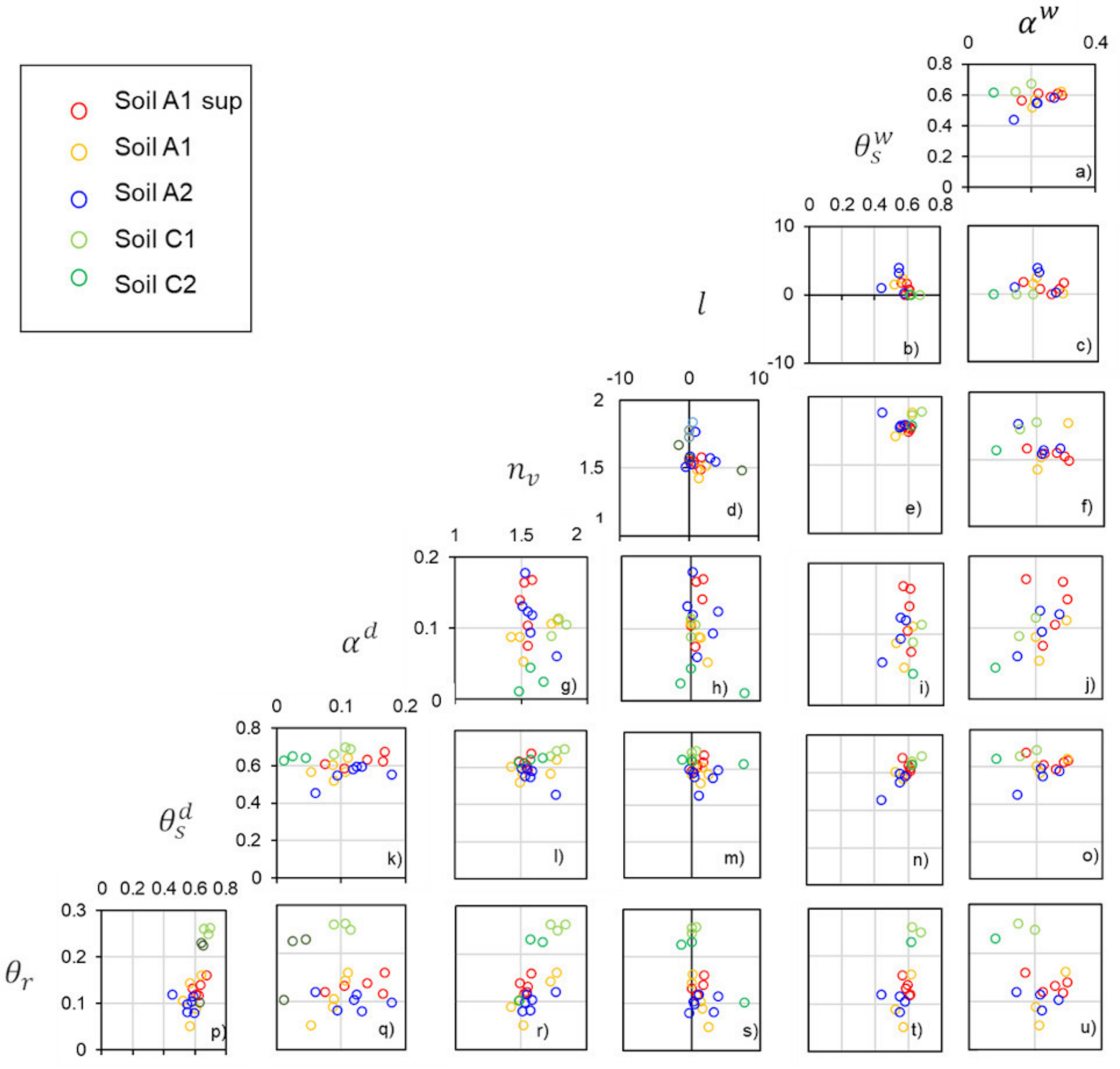
Soil A1 sup
Soil A1
Soil A2
Soil C1
Soil C2
α^w
θ_S^w
l
n_v
α^d
θ_S^d
θ_r
a)
b)
c)
d)
e)
f)
g)
h)
i)
j)
k)
l)
m)
n)
o)
p)
q)
r)
s)
t)
u)

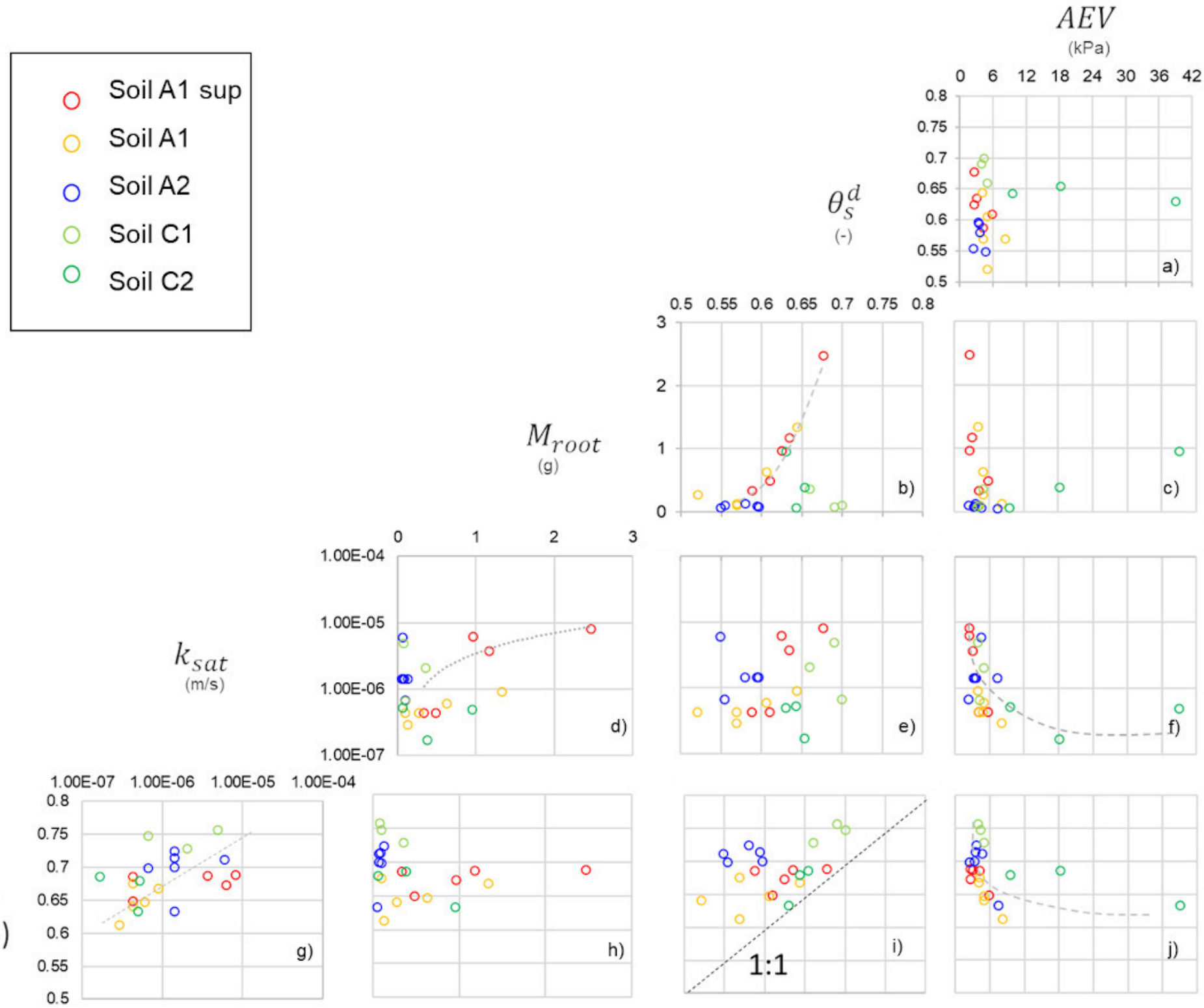
Soil A1 sup
Soil A1
Soil A2
Soil C1
Soil C2
AEV
(kPa)
0 6 12 18 24 30 36 42
θ_s^d
(-)
0.8
0.75
0.7
0.65
0.6
0.55
0.5
a)
0.5 0.55 0.6 0.65 0.7 0.75 0.8
M_{root}
(g)
3
2
1
0
b)
c)
0 1 2 3
k_{sat}
(m/s)
1.00E-04
1.00E-05
1.00E-06
1.00E-07
d)
e)
f)
1.00E-07 1.00E-06 1.00E-05 1.00E-04
n
(-)
g)
h)
i)
1:1
j)

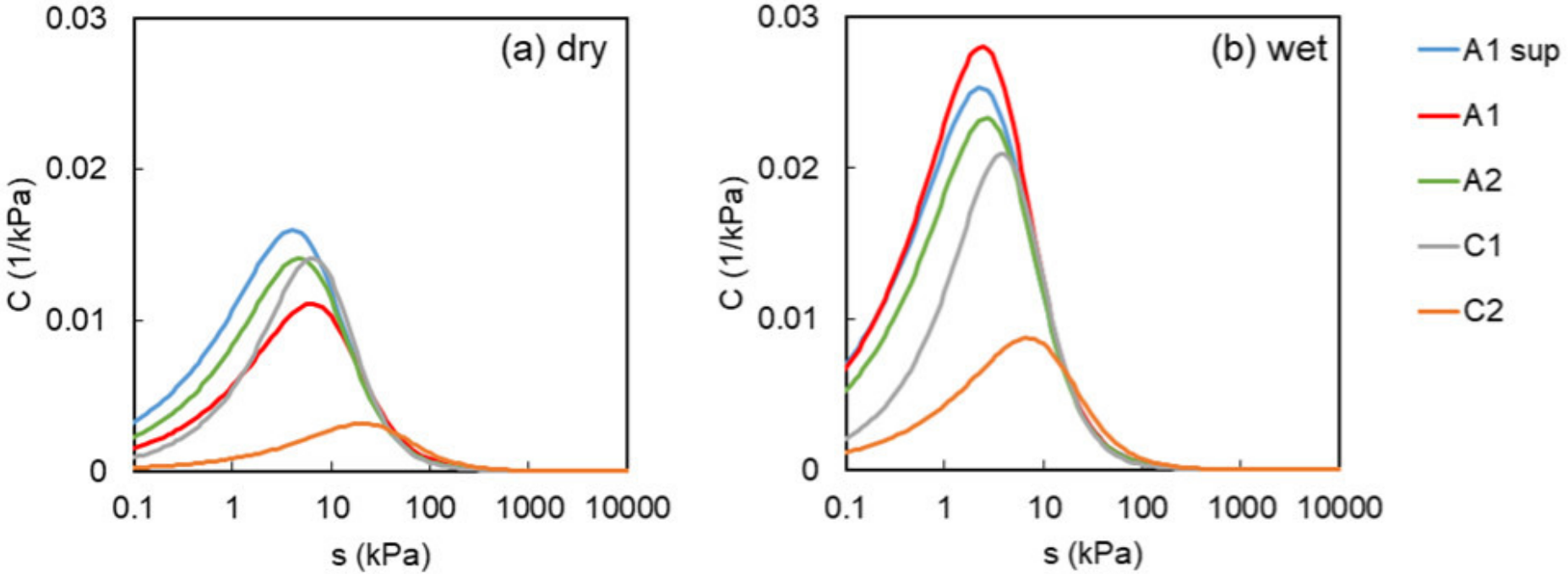
(a) dry
(b) wet
C (1/kPa)
s (kPa)
0.03
0.02
0.01
0
0.1
1
10
100
1000
10000
A1 sup
A1
A2
C1
C2

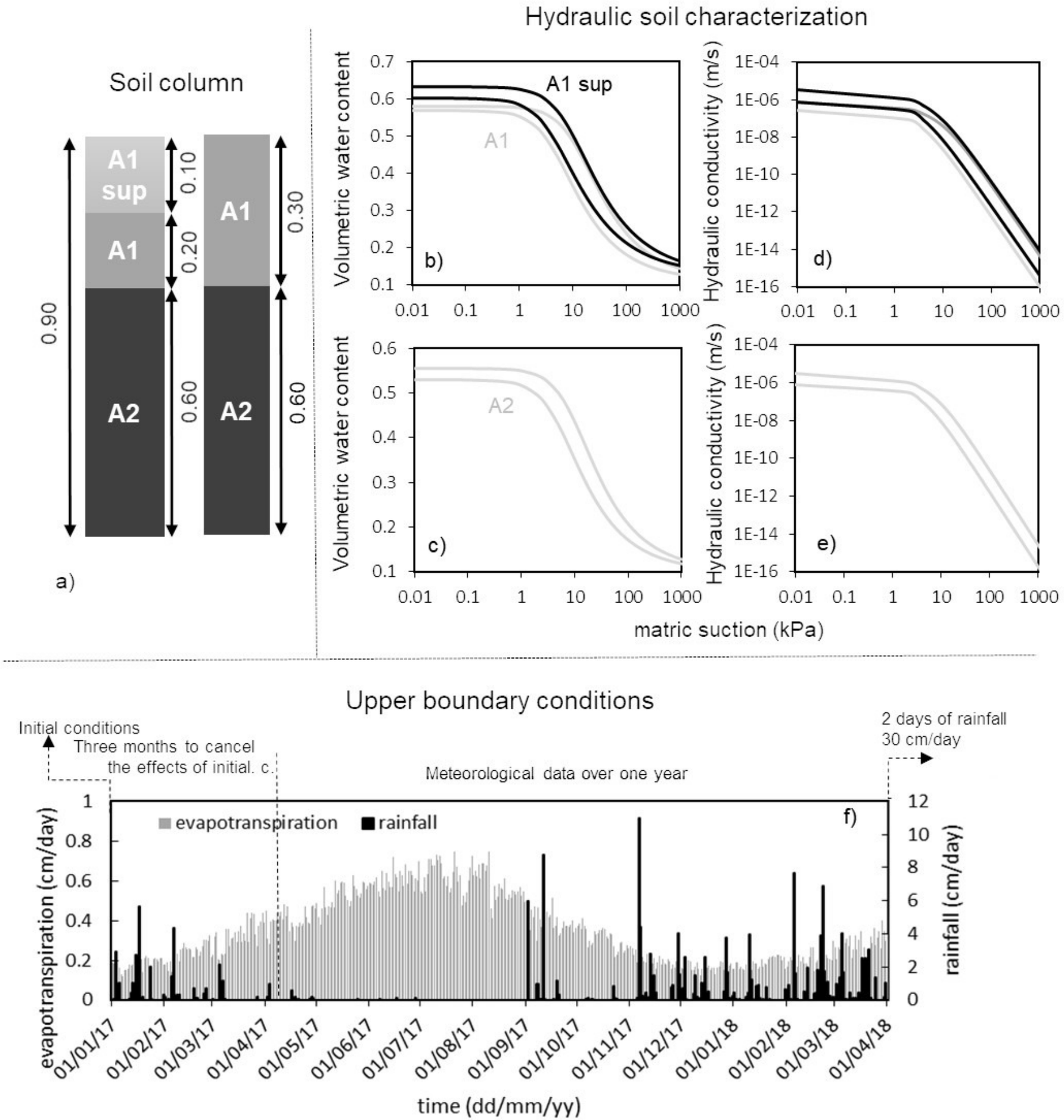
Soil column
A1 sup
A1
A2
A1
A2
0.90
0.10
0.20
0.60
0.30
0.60
a)
Hydraulic soil characterization
Volumetric water content
A1 sup
A1
b)
Hydraulic conductivity (m/s)
d)
A2
c)
e)
matric suction (kPa)
Upper boundary conditions
Initial conditions
Three months to cancel
the effects of initial. c.
Meteorological data over one year
2 days of rainfall
30 cm/day
evapotranspiration
rainfall
f)
evapotranspiration (cm/day)
rainfall (cm/day)
time (dd/mm/yy)
01/01/17
01/02/17
01/03/17
01/04/17
01/05/17
01/06/17
01/07/17
01/08/17
01/09/17
01/10/17
01/11/17
01/12/17
01/01/18
01/02/18
01/03/18
01/04/18

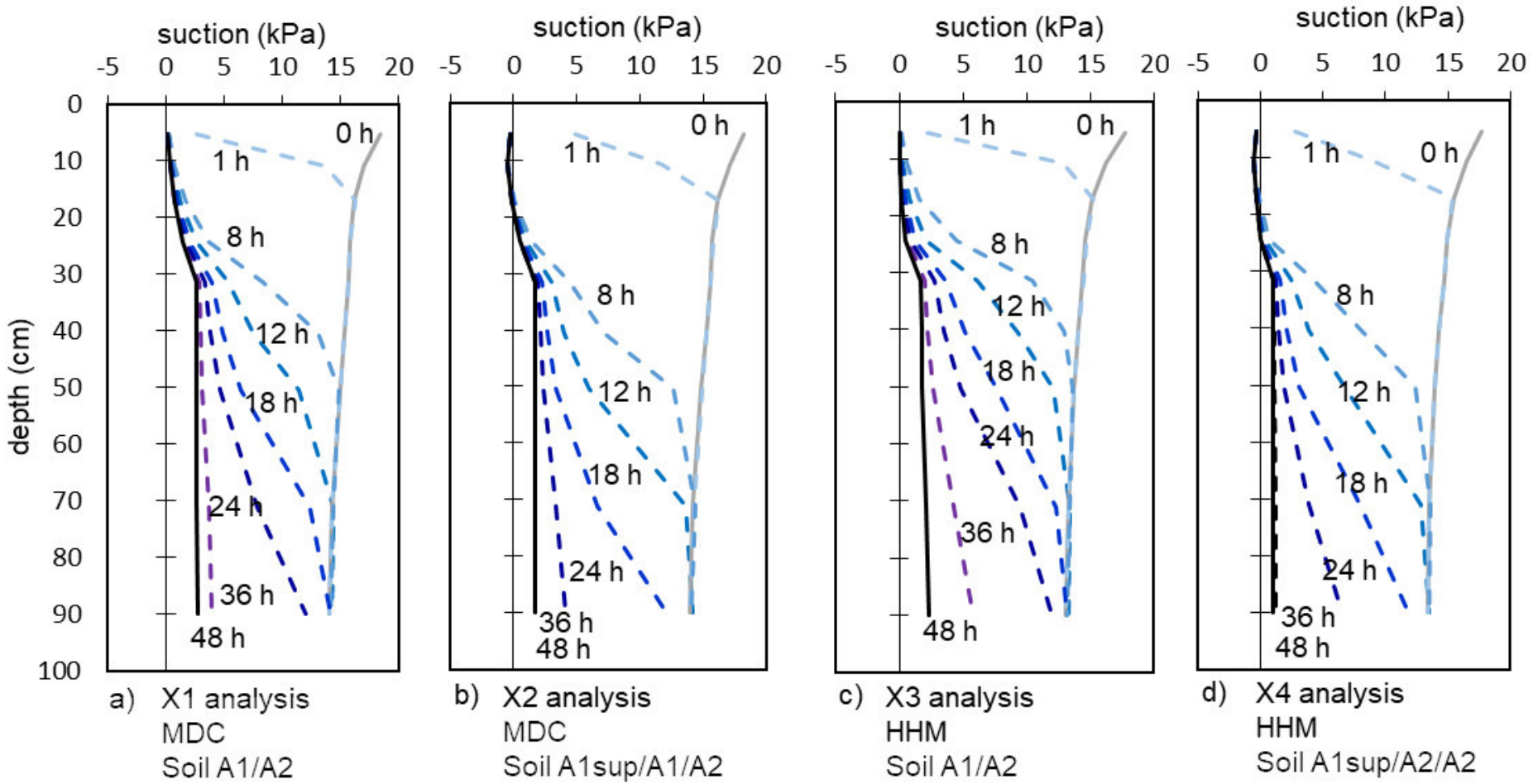
suction (kPa)
-5 0 5 10 15 20
depth (cm)
0 10 20 30 40 50 60 70 80 90 100
0 h
1 h
8 h
12 h
18 h
24 h
36 h
48 h
a) X1 analysis
MDC
Soil A1/A2
b) X2 analysis
MDC
Soil A1sup/A1/A2
c) X3 analysis
HHM
Soil A1/A2
d) X4 analysis
HHM
Soil A1sup/A2/A2

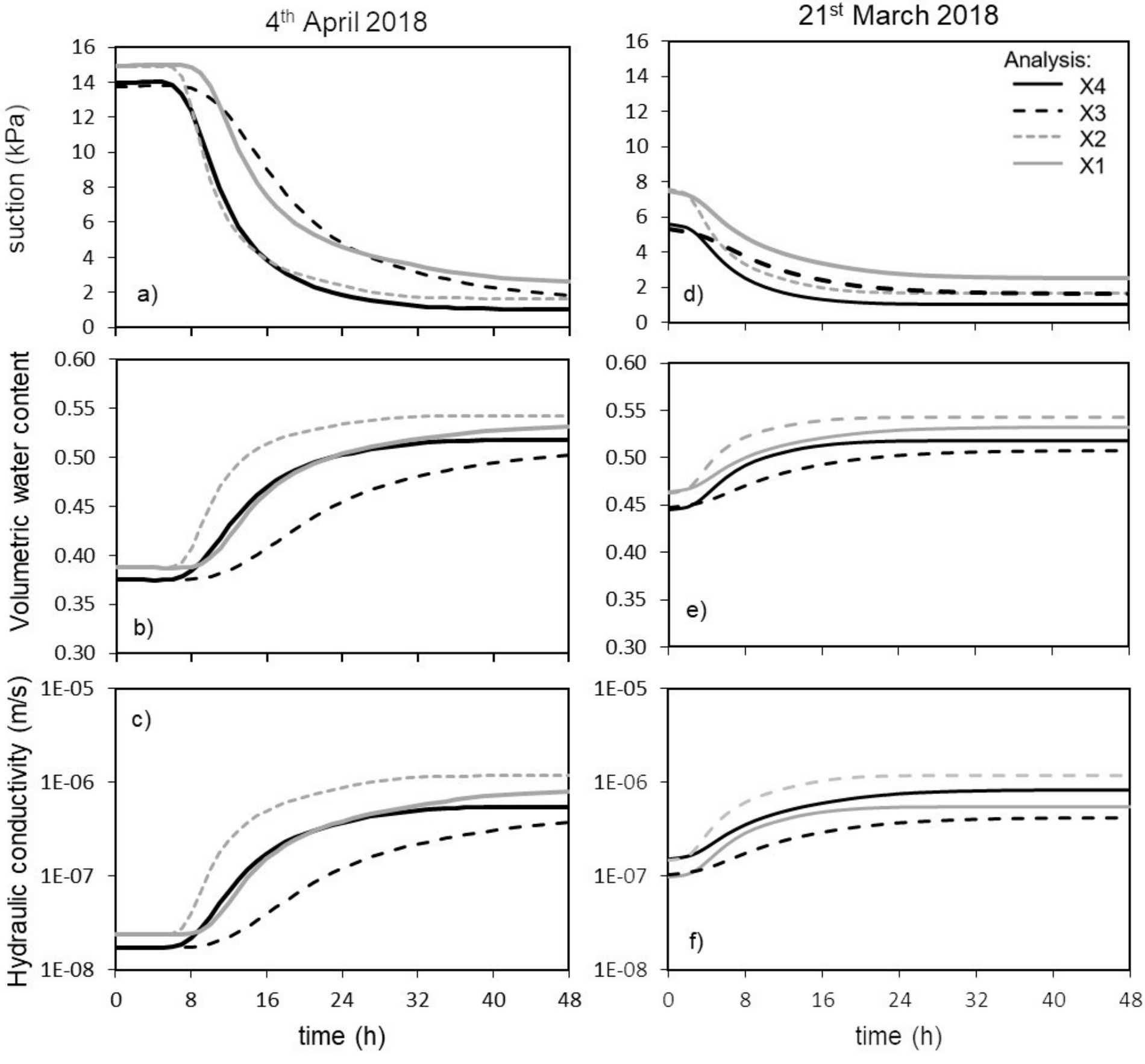
4th April 2018
21st March 2018
suction (kPa)
Volumetric water content
Hydraulic conductivity (m/s)
time (h)
time (h)
Analysis:
X4
X3
X2
X1
a)
b)
c)
d)
e)
f)
16
14
12
10
8
6
4
2
0
0.60
0.55
0.50
0.45
0.40
0.35
0.30
1E-05
1E-06
1E-07
1E-08
0
8
16
24
32
40
48

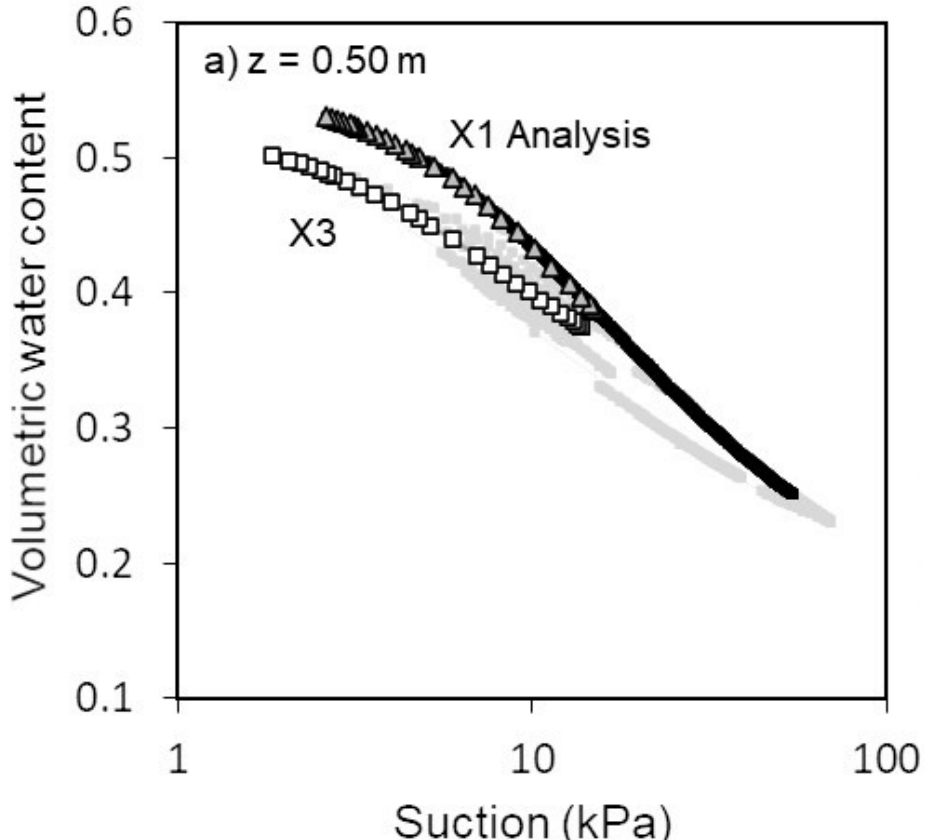
a) z = 0.50 m
X1 Analysis
X3
Volumetric water content
0.6
0.5
0.4
0.3
0.2
0.1
1
10
100
Suction (kPa)

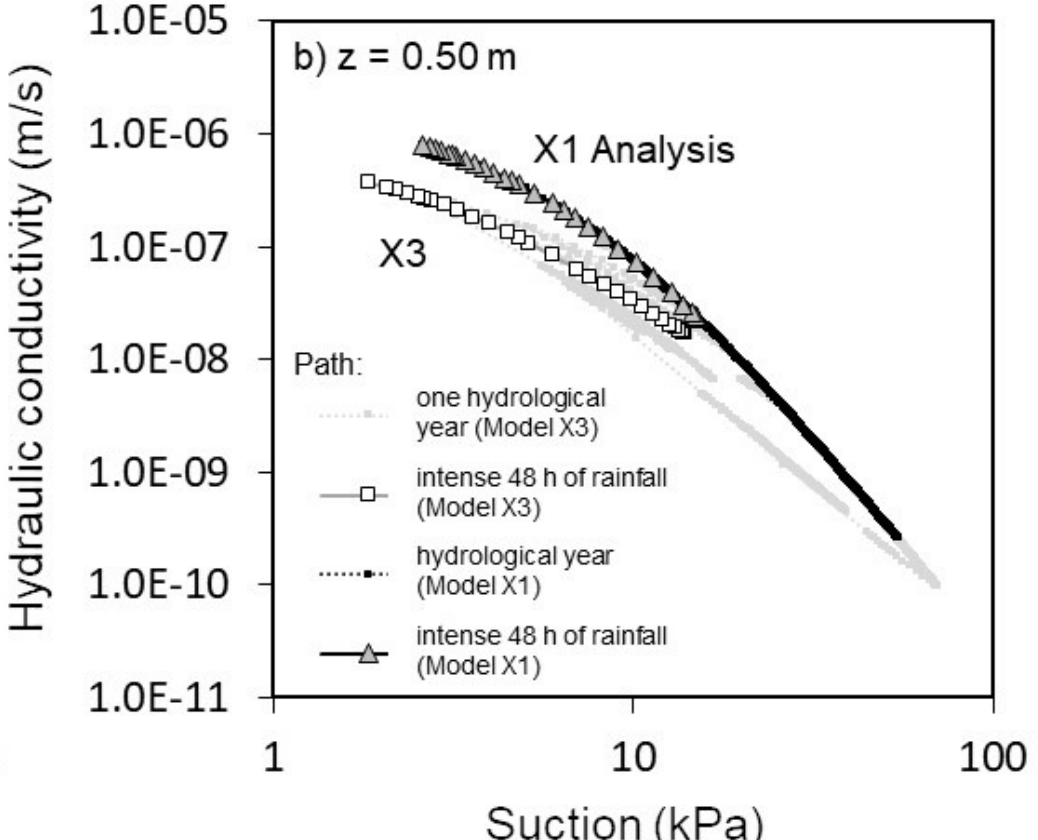
b) z = 0.50 m
X1 Analysis
X3
Hydraulic conductivity (m/s)
1.0E-05
1.0E-06
1.0E-07
1.0E-08
1.0E-09
1.0E-10
1.0E-11
Path:
one hydrological year (Model X3)
intense 48 h of rainfall (Model X3)
hydrological year (Model X1)
intense 48 h of rainfall (Model X1)
1
10
100
Suction (kPa)